

1 Dear Editors and Referees:

2
3 Thank you for your letter and for the referees' comments concerning our
4 manuscript entitled "Modeling study on the transport of summer dust and
5 anthropogenic aerosols over the Tibetan Plateau". Those comments are
6 all valuable and very helpful for revising and improving our paper, as
7 well as the important guiding significance to our researches. We have
8 studied the comments carefully and have made correction which we hope
9 meet with approval. Revised portion are marked in the document named
10 "manuscript_make_up". The main corrections in the paper and our point-
11 by-point responses to the referee's comments are as flowing:

12
13
14 **Referee #1**

15
16 **General comments:**

17 This study describes the transport processes of dust and anthropogenic
18 aerosols over the Tibetan Plateau by the simulation using an aerosol
19 transport model coupled with a non-hydrostatic regional model. It is
20 worthwhile to clarify the transport processes because the aerosols over
21 the Tibetan Plateau arrive at the high altitude and spread in the wide
22 range. However, there are ambiguous descriptions in the paper. It is better
23 to indicate the locations of the northern and southern slopes, and the east
24 area of the Tibetan Plateau in the figures. I recommend publication after
25 the revisions.

26
27 **Specific comments:**

28 1. 15013, L4-5: Two locations of Taklimakan desert are written,
29 "Northeast of TP, Taklimakan desert" and "West of TP, the Taklimakan
30 Desert".

31 **Response:**

32 We are very sorry for our ambiguous descriptions. In fact, we wanted to
33 express that the Taklimakan desert is the important dust source not only
34 for west of TP but also for northwest of TP. However, the correct

35 meaning was not described in this manuscript.

36 To express more accurately, we change ‘Northeast of the TP’ to ‘For the
37 northeast of TP’ and change ‘West of the TP’ to ‘For the west of TP’
38 (15013, L4-6 in “Revised manuscript--response to the referees”; line 223-
39 225 in “manuscript_make_up”).

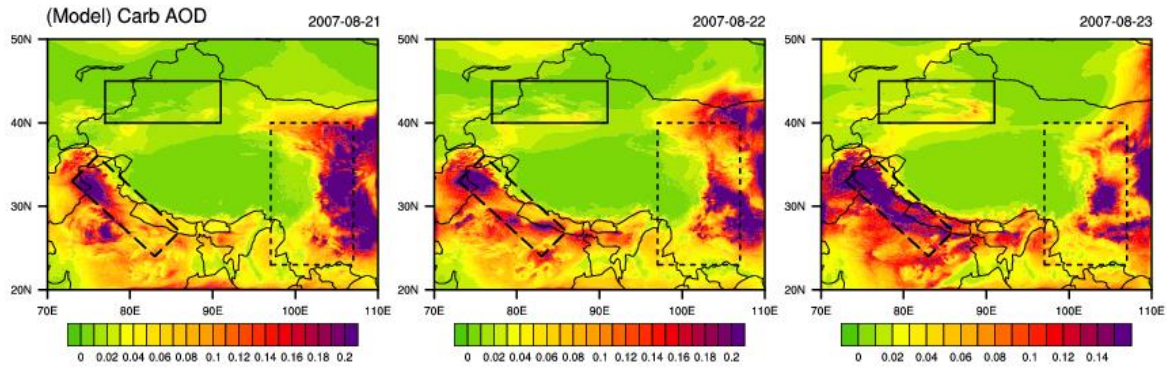
40

41 2. 15015, L16: Where is the area of “the decreasing SSA and AE over the
42 northern slope of the TP” in Figure 4? The solid box? The SSA decreases
43 but the AE increase in the solid box. Furthermore, the AOD (Figure 3b)
44 and the mass column loading of dust (Figure 9) are small in the solid box.
45 What is the aerosol in the solid box?

46 **Response:**

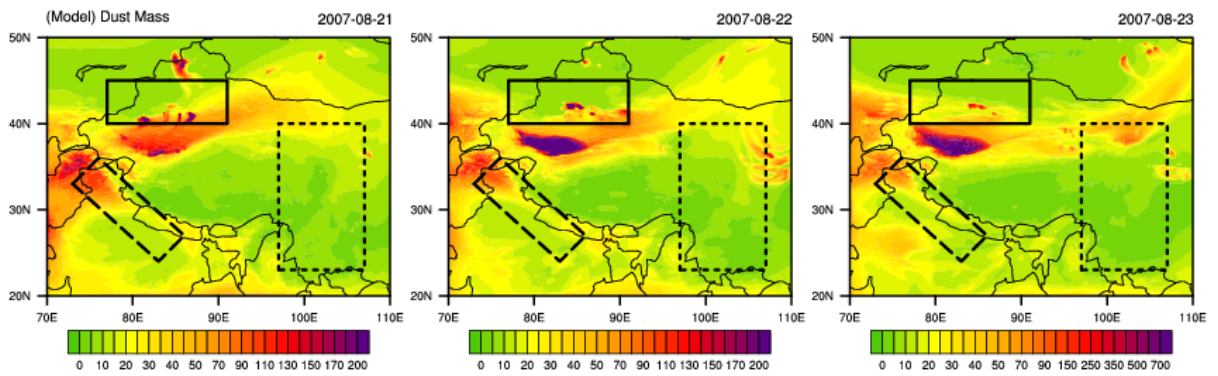
47 The area of ‘the decreasing SSA and increasing AE’ is the solid box in
48 Fig. 4 and so we delete ‘over the northern slope of the TP’ (15015, L16-
49 17 in “Revised manuscript--response to the referees”; line 293-294 in
50 “manuscript_make_up”). In order to show the transport of dust visually,
51 we use the uniform color bar for the three days. However, the uniform
52 color bar may cover up some details of some relative smaller values. To
53 present more clearly, here, we show the simulated AOD and mass column
54 loading of dust in different color bar for three days. As shown in Figures
55 B1-B2, the dust aerosols and carbon suggest eastward-moving trend in
56 the solid box, which may be the reason of the changes of SSA and AE in
57 solid box. Furthermore, for accurately, orbit-altitude cross section of
58 feature classifications from CALIPSO (Cloud-Aerosol Lidar and Infrared
59 Pathfinder Satellite Observation) Level 2 Aerosol Layer and Vertical
60 Feature Mask (VFM) products is given in Figure B3. As shown in Figure

61 B3, the main component of aerosols in the solid box is polluted dust. It
 62 could be concluded that there are large numbers of dust aerosols and
 63 some of these dust particles have been polluted by carbon.



64

65 **Figure B1** Distributions of the simulated AOD of carbon from 21-23 August 2007

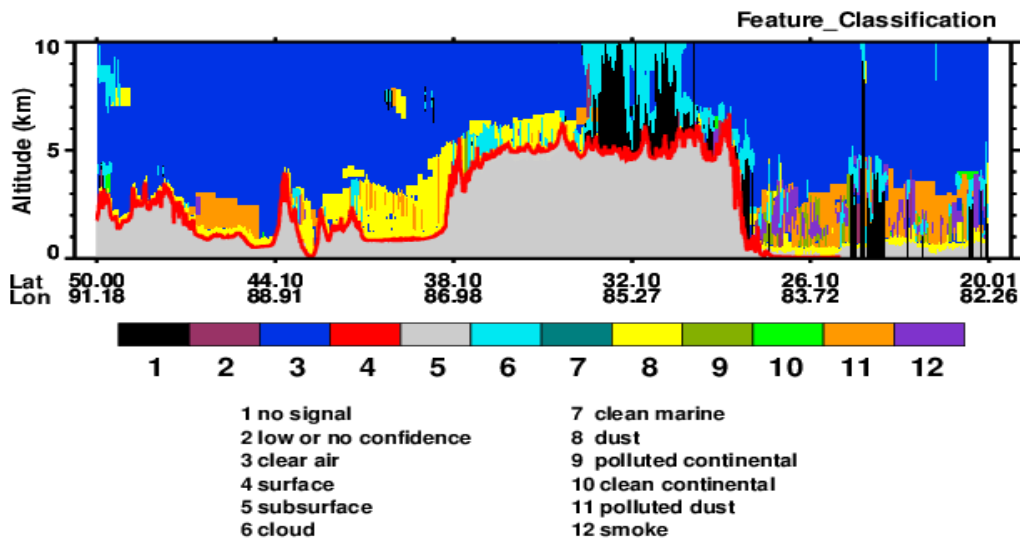


66

67 **Figure B2** Distributions of the simulated dust mass column loading (units: mg m^{-2}) from 21-23

68

August 2007.



69

70 **Figure B3.** Feature classifications of particles in the atmosphere on 22 August 2007 along the
71 trajectory of the CALIPSO satellite indicated in Figure 1

72
73 3. 15015, L21-23: The SSA of the dust regions shown in Figures 3 and 9
74 is high in Figure 4a. The high SSA regions spreads eastward in Figure 4a.

75 **Response:**

76 ‘The simulation suggests that the eastward and southward migration of
77 dust aerosols induced the declining SSA over the northern slope and east
78 of the TP’ is changed to ‘The simulation suggests that the eastward and
79 southward migration of dust aerosols induced the increasing SSA over the
80 northern slope and east of the TP, respectively (15015, L21-23 in
81 “Revised manuscript--response to the referees”; line 298-301 in
82 “manuscript_make_up”).

83
84 4. Figure 5: The topography of the southern slope of the TP is very
85 different between Figures 5a and b. Is this due to the model resolution?

86 **Response:**

87 Yes, the limitation of model resolution induces the obvious differences of
88 the topography between Figures 5a and b. Considering the computation
89 pressure of SPRINTARS added to NHM and the minor difference of
90 aerosol properties in different model resolution, we set the model
91 resolution shown in manuscript and the simulated result does describe the
92 horizontal and vertical distributions of aerosol.

93
94 5. 15017, L27-28: What is “whereas another current curves northeast”?

95 **Response:**

96 We intended to mean that northwesterly current from Kazakhstan turn
97 into two branches when it reaches the east side of Tianshan Mountain,
98 while One current branch moves to the east continuously and another
99 branch turns to northeasterly wind toward the TP because of topographic
100 blocking due to the high elevation. To describe it more accurately, we
101 change ‘whereas another current curves northeast’ to ‘whereas another
102 current turns into northeasterly wind toward the TP’ (15017, L27-28 in
103 “Revised manuscript--response to the referees”; line 367-369 in
104 “manuscript_make_up”).

105

106 6. 15018, L15-16: Is the westerly wind correct? I cannot understand what
107 you mean.

108 **Response:**

109 We are appreciated for your comments and sorry for such a simple
110 mistake. And ‘a westerly wind’ is changed to ‘easterly wind’ (15018, L16
111 in “Revised manuscript--response to the referees”; line 386 in
112 “manuscript_make_up”).

113

114 7. 15018, L18-15019, L21: The dust mass concentration is depicted in
115 Figures 8 and “aerosol mass concentration” should be changed to “dust
116 mass concentration”.

117 **Response:**

118 Thanks for the referee’s kind advice and we have made correction
119 according to the referee’s comments. All these ‘aerosol mass
120 concentration’ have been changed to ‘dust mass concentration’ (15018,
121 L18; 15019, L16 in “Revised manuscript--response to the referees”; line
122 388, 418, in “manuscript_make_up”).

123

124 8. 15018, L27: Is “9 km” correct? The dust cannot be observed at 9km in
125 Figures 8a2 and b2.

126 **Response:**

127 To express more accurately, we have modified this sentence. (15018,
128 L26-28 in “Revised manuscript--response to the referees”; line 397-401
129 in “manuscript_make_up”)

130 ‘On 22 August, the dust was transported upward to 9 km, and the aerosol
131 mass concentration around the outbreak location weakened (Fig. 8a2).’

132 is changed to

133 ‘With the development and transportation of the dust particles in the
134 following two days, the particles were transported to higher and even
135 upward to 9 km (Fig. 8a3 and 8b3).’

136

137 9. 15018, L28: Where is the outbreak location in Figure 8a2.

138 **Response:**

139 In this version, we wanted to mean that the outbreak location is the place
140 where the dust event began to outbreak on 21 August (at approximately
141 78°E, 37°N). However, according to the comments from **Referee #2**, “**The**
142 **dust simulations and its spatial extent around 40N shown in Figure 3**
143 **does not very well compared with OMI observations**”, the simulation
144 was re-conducted with a tuned parameter for regional model. Basing on
145 the new result, we modified this sentence to be ‘With the development
146 and transportation of the dust particles in the following two days, the
147 particles were transported to higher and even upward to 9 km (Fig. 8a3
148 and 8b3).’(15018, L26-28 in “Revised manuscript--response to the
149 referees”; line 397-401 in “manuscript_make_up”)

150

151

152 10. 15018, L28: Where is the dust transported eastward from 70 to 80E in
153 Figure 8a2?

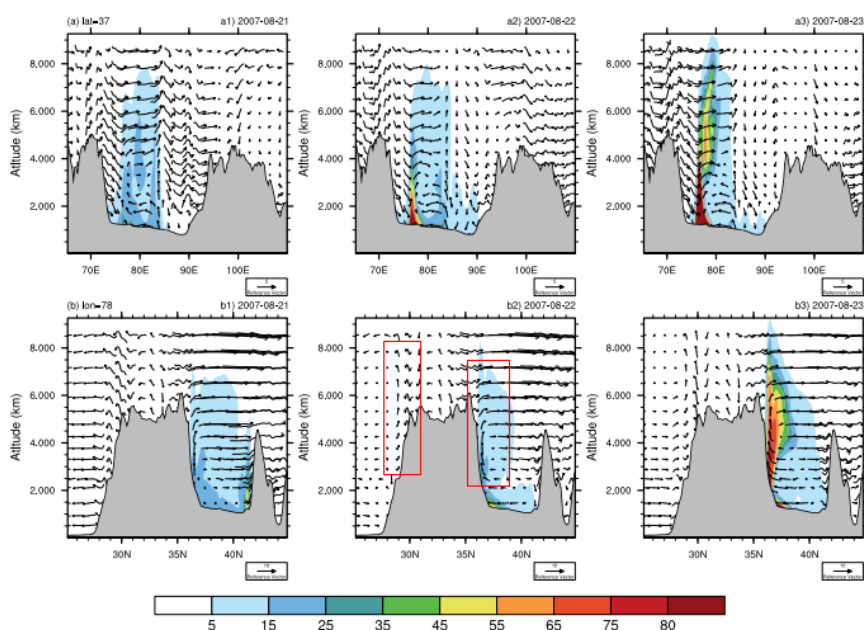
154 **Response:**

155 We have changed ‘from 70 to 80 °E’ to ‘over the region from 70 to 80 °E’
156 (15018, L28 in “Revised manuscript--response to the referees”; line 402
157 in “manuscript_make_up”).

158 11. 15019, L4: The large updraft near the southern slope of TP is not
159 observed in Figures 8b.

160 **Response:**

161 Although it is weaker than the updraft near the northern slope of TP, the
162 updraft still can be found over the southern slope of TP, as the red boxes
163 shown in Fig. B4.



164

165 **Figure B4.** Cross-section of the (a) vertical-longitude and (b) vertical-latitude distributions of
 166 the simulated dust mass concentration and wind vectors from 21 to 23 August 2007.

167 12. 15019, L10: “the east area of the TP”

168 **Response:**

169 Here, we want to distinguish that the area we analyzed is located in the
 170 east of the TP instead of part of the TP, so we think ‘the area east of the
 171 TP’ shouldn’t be replaced by ‘the east area of the TP’.

172

173 13. 15019, L16: Where do the aerosols begin to extend southeastward?

174 The northern or southern slopes?

175 **Response:**

176 We have rewritten this sentence (15019, L16-17 in “Revised manuscript--
 177 response to the referees”; line 418-421 in “manuscript_make_up”).

178 ‘The aerosol mass concentration began to increase and extend
 179 southeastward on 21 August.’ is changed to ‘With the development and
 180 transportation, dust mass concentration over the northern slope began to
 181 increase and extend southeastward on 21 August’.

182

183

184 **Reviewer #2**

185

186 **Comments: The paper addressed the evaluation of SPRINTARS**
187 **using satellite observations. SPRINTARS must have been evaluated**
188 **previously by several investigators. Also, there is no novel idea was**
189 **addressed which merits the publication of this version in ACP.**
190 **However, it may be considered if the authors address the following**
191 **issues:**

192 **Response:** Thank you for your comments. As you mentioned,
193 SPRINTARS has been evaluated by many previous studies, and its
194 performance was well confirmed for "Global Scale Simulation", whose
195 grid resolution is usually a hundred to several hundreds km.

196 However it has not been implemented into "regional scale model" until
197 now. In this study, SPRINTARS is firstly implemented "regional scale
198 model" called NHM (Saito et al. 2006).

199 The weakness of Global Climate Models is low resolution and neglecting
200 the complex geomorphic types, different natural conditions and human
201 activities. Regional climate models have higher resolutions and they can
202 characterize the terrain and the surface condition better.

203 Generally speaking, there are a large amount of tunings and
204 parameterizations in aerosol modules, and it is not always clear whether
205 these tunings and parameterization work well or not in regional scale
206 model. In this point, SPRINTARS is no exception.

207 In this sense, it is very important to confirm the validity of the
208 SPRINTARS coupled with regional scale model with 20 km grid
209 resolution, and we think that this study is very important for showing the
210 performance of SPRINTARS in regional model for the first time.

211 The validity of the SPRINTARS coupled with regional scale model will
212 ameliorate the regional simulations from global climate model and
213 increase the simulating accuracy of regional climate change.

214

215 **Comments: The dust simulations and its spatial extent around 40N**
216 **shown in Figure 3 does not very well compared with OMI**
217 **observations.**

218 **Response:** Thank you for your comments. There really exists some
219 underestimation in the simulations with the dust emission parameter used
220 in GCM model. We have re-run the model with the tuned the parameter
221 of dust emission and the corresponding results (figures 3-9 in the
222 manuscript) have been given in the document 'figures'.

223

224 **Comments: Also, model overestimates the carbonaceous and sulfate**
225 **aerosol distribution around 100E. The reasons why it is not matching**
226 **with observations are not explained clearly.**

227 **Response:** First of all, we think that the aerosol distribution around 100° E
228 is not bad, and there are many missing value in observation data around
229 this area. We can add some word for this reason. From the available
230 satellite data, we think the agreement with simulation is not bad. Does the
231 reviewer indicate aerosol distribution east to 105°E? If so, we think that
232 one of the reasons of the overestimation is the effect of lateral boundary.
233 In generally, results of the regional scale model, into which SPRINTARS
234 firstly implemented by this study, are affected by artificial wave and
235 artificial noise around lateral boundary. These noises also affect the
236 advection of aerosol, and therefore spatial distribution of aerosol.

237 All of the regional scale models have the problem of lateral boundary,
238 and we omitted the discussion on the results around lateral boundary.

239

240 Some minor suggestions

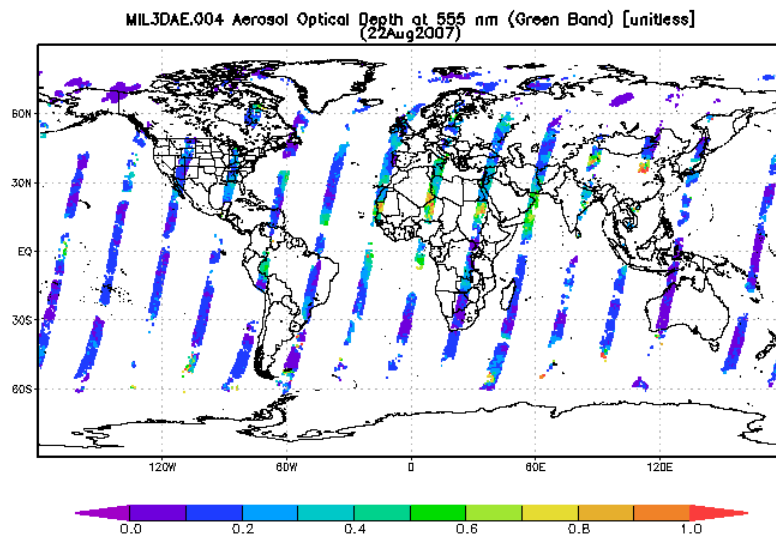
241 **Comments: Page # 15013 Line 19: Rainclouds may be corrected as**
242 **"warm clouds"**

243 **Response:** Sorry for our mistake. The word "rainclouds" should be
244 "raindrops" or "cloud droplets". We modified this word in revised
245 manuscript (15013 Line 19 in "Revised manuscript--response to the
246 referees"; line 239 in "manuscript_make_up").

247

248 **Comments: Page # 15016 Line 14: "Considering the missing satellite**
249 **observations over 21-23 August". You have used MISR, OMI and**
250 **which data was missing?**

251 **Response:** We are very sorry for our ambiguous descriptions. The MISR
252 orbit can only cover 360 km wide and there exist plenty of missing
253 observations in daily products (as shown in Fig. B1). In order to evaluate
254 SPRINTARS combined with NHM, we compared the simulated monthly
255 aerosol optical properties with the MISR observations.
256 To express more accurately, we rewrite this sentence and ‘Considering
257 the missing satellite observations over 21–23 August, we compared the
258 simulated monthly aerosol optical properties with the MISR observations
259 on August 2007 over the TP’ is changed to ‘Considering the missing
260 observations of MISR, we compared the simulated monthly aerosol
261 optical properties with the satellite observations on August 2007 over the
262 TP’ (15016 Line 14-16 in “Revised manuscript--response to the referees”;
263 line 322-326 in “manuscript_make_up”).



264

265 Fig. B1 Aerosol optical depths at 555nm on 22 August 2007 from the MISR.

266 **Comments: In some places it is spelled as "Taklimakan" instead of**

267 **"Taklamakan"**

268 **Response:** Sorry for our negligence. These two words both mean the

269 largest desert in China, filling the Tarim Basin. In order to unify the

270 writing, all of these words "Taklamakan" are changed to "Taklimakan".

271 We modify the spells in revised manuscript (15017 Line 11, 14 in

272 "Revised manuscript--response to the referees"; line 350, 353 in

273 "manuscript_make_up").

274

275 **Author's changes :**

276

277 We have checked the manuscript and have corrected several spelling and

278 formatting mistakes (Line 103, 184, 237, 246, 255, 264, 328, 431, 452,

279 577-579, 762, 825 in “manuscript_make_up”). To express convincingly,
280 we also added several references in the manuscript (Line 572-576, 660-
281 662 in “manuscript_make_up”).

282

283

284 Special thanks to you for your good comments.

285

286 We have checked the manuscript and revised it according to the
287 comments. We submit here the revised manuscript as well as a
288 list of changes. We hope that the revised version of the paper
289 has addressed much of the referee’s concerns and is now
290 acceptable for publication.

291

292 If you have any question about this paper, please don't hesitate
293 to contact me at the address below.

294 Thank you and best regards.

295 Sincerely yours,

296 Yuzhi Liu

297

298 Corresponding author:

299 Name: Yuzhi Liu

300 E-mail: liuyzh@lzu.edu.cn

301

302 **Modeling study on the transport of summer dust and**
303 **anthropogenic aerosols over the Tibetan Plateau**

304

305 **Y. Liu¹, Y. Sato², R. Jia¹, Y. Xie¹, J. Huang¹, T. Nakajima³**

306

307

308

309

310 ¹ Key Laboratory for Semi-Arid Climate Change of the Ministry of Education,
311 College of Atmospheric Sciences, Lanzhou University, Lanzhou, 730000, China

312 ² Advanced Institute for Computational Science, RIKEN, Kobe, Hyogo, 6500047,
313 Japan

314 ³ Earth Observation Research Center, JAXA, Tsukuba, Ibaraki, 3058505, Japan

315 Correspondence to: Y. Liu (liuyzh@lzu.edu.cn)

316

317

318

319

320

321

322

323

324

Abstract

325 The Tibetan Plateau (TP) is located at the juncture of several important natural and
326 anthropogenic aerosol sources. Satellites have observed substantial dust and
327 anthropogenic aerosols in the atmosphere during summer over the TP. These aerosols
328 have distinct effects on the earth's energy balance, microphysical cloud properties,
329 and precipitation rates. To investigate the transport of summer dust and anthropogenic
330 aerosols over the TP, we combined the Spectral Radiation-Transport Model for
331 Aerosol Species (SPRINTARS) with a non-hydrostatic regional model (NHM). The
332 model simulation shows heavily loaded dust aerosols over the northern slope and
333 anthropogenic aerosols over the southern slope and to the east of the TP. The dust
334 aerosols are primarily mobilized around the Taklimakan Desert, where a portion of
335 the aerosols are transported eastward due to the northwesterly current; simultaneously,
336 a portion of the particles are transported northward when a second northwesterly
337 current becomes northeasterly because of the topographic blocking of the northern
338 slope of the TP. Because of the strong upward current, dust plumes can extend
339 upward to approximately 7-8 km a.s.l. over the northern slope of the TP. When a dust
340 event occurs, anthropogenic aerosols that entrain into the southwesterly current via
341 the Indian summer monsoon are transported from India to the southern slope of the
342 TP. Simultaneously, a large amount of anthropogenic aerosols is also transported from
343 eastern China to east of the TP by easterly winds. An investigation on the transport of
344 dust and anthropogenic aerosols over the plateau may provide the basis for
345 determining aerosol impacts on summer monsoons and climate systems.

346 Key words: dust, transport, anthropogenic aerosols, Tibetan Plateau

347

348

349

350

351

352 1 Introduction

353 Aerosols, which primarily comprise a mixture of soil dust, sulfate, carbonaceous
354 material and sea salt, may have a large, direct effect on the energy balance by
355 absorbing and scattering solar and thermal radiation (Liu et al., 2011, 2014; Miller
356 and Tegen, 1998, 2003) and an indirect effect on the microphysical properties of
357 clouds (DeMott et al., 2003; Huang et al., 2010). Mineral dust, which is the main
358 component of aerosols, is a primary type of absorbing aerosol ([Huang et al., 2007a](#);
359 [Huang et al., 2011](#); Sokolik and Toon, 1996). Asia dust (Hsu et al., 2013; Nakajima et
360 al., 2003) and anthropogenic aerosols create a significant environmental problem
361 when mixed during transport (Takemura et al., 2002). Asia dust, which generally
362 originates from Outer and Inner Mongolia, the Taklimakan Desert, and the Gobi
363 Desert, and anthropogenic aerosols can be transported eastward by the jet stream to
364 North America across the North Pacific Ocean (Gong et al., 2006; Takemura et al.,
365 2002; Uno et al., 2001).

366 Atmospheric aerosols are dispersed worldwide (Breider et al., 2014; Goudie and
367 Middleton, 2001; Müller et al., 2003). Recent studies indicate that dust aerosols
368 accumulate over the northern slope of the Tibetan Plateau (TP) (Chen et al., 2013;
369 [Huang et al., 2007b](#)). As the highest plateau in the world, the TP may influence the
370 climate through dynamical and thermal forcing (Wu et al., 2007) and by modulating
371 the hydrologic cycle (Hansen et al., 2000; Jacobson, 2001). The TP is located at the
372 juncture of several important natural and anthropogenic aerosol sources and is
373 surrounded by the earth's highest mountains, e.g., the Himalayas and the Pamir and
374 Kunlun Mountain ranges; the Taklimakan Desert lies to the north, the Gobi Desert lies
375 to the northeast and the Great Indian Desert lies to the southwest. With an increasing
376 frequency of nearby dust storms (Thulasiraman et al., 2002; Uno et al., 2001), the TP
377 faces new threats from aerosols.

378 As the major type of aerosol that affects the TP ([Huang et al., 2007b](#); Zhang et al.,
379 2001), dust aerosols accumulate on the northern slope of the plateau, where the
380 Taklimakan and Gobi Deserts intersect. From April to May, dust aerosols, which are

381 transported from the Pakistan/Afghanistan, the Middle East, the Sahara, and
382 Taklimakan Deserts, accumulate at high elevations on the southern and northern
383 slopes of the TP (Lau et al., 2006). The largest number of dust storms occurred over
384 the northern slope and eastern part of the TP in the spring of 2007, and several dust
385 layers were elevated to altitudes of 11-12 km (Liu et al., 2008). During summer, dust
386 aerosol particles are transported from nearby deserts, such as the Taklimakan Desert,
387 and accumulate on the northern and southern slopes of the TP. Tibetan dust aerosol
388 layers appear most frequently at approximately 4-7 km above the mean sea level,
389 where the plumes likely originate from the nearby Taklimakan Desert and accumulate
390 over the northern slopes of the TP during summer (Huang et al., 2007**b**). As the dust
391 storm travels toward the TP, the dust aerosols may mix with anthropogenic aerosols
392 (Takemura et al., 2002) and induce new environmental and climatic problems [\(Su et](#)
393 [al., 2008\)](#).

394 The elevated absorbing aerosols have a unique feedback with the high surface
395 albedo of the TP (Liu et al., 2013). According to a modeling study, the atmosphere in
396 the upper troposphere over the TP may act as an “elevated heat pump” (Lau and Kim,
397 2006), which can be affected by the absorption of solar radiation by dust coupled with
398 black carbon emitted from industrial areas in northern India; this setup may advance
399 and subsequently intensify the Indian monsoon. However, the Tibetan aerosol
400 distribution and properties are largely unknown.

401 In this study, we firstly evaluated the Spectral Radiation-Transport Model for
402 Aerosol Species (SPRINTARS) combined with a non-hydrostatic regional model
403 (NHM) through comparing the simulation results and satellite observations, including
404 the altitude-orbit cross-section of the extinction coefficient along the trajectory of
405 Cloud-Aerosol Lidar and Infrared Pathfinder Satellite Observations (CALIPSO), the
406 aerosol index (AI) in the ultraviolet (UV) band from an ozone monitoring instrument
407 (OMI), and monthly aerosol optical depth (AOD) data from a multi-angle imaging
408 spectroradiometer (MISR). Simultaneously, the dust and anthropogenic aerosols in
409 summer over the TP are evaluated, and their distributions over the TP are presented.

410 The transport of these aerosols is also explored via combining the simulation results
411 and reanalysis data.

412

413 **2 Model description**

414 **2.1 Adding SPRINTARS to the NHM**

415 The three-dimensional aerosol transport-radiation model called SPRINTARS
416 (Takemura et al., 2000, 2002) is used in this study. This global aerosol climate model
417 was developed at the Center for Climate System Research (CCSR), University of
418 Tokyo. The model simultaneously considers the main tropospheric aerosols, i.e.,
419 carbon (organic carbon (OC) and black carbon (BC)), sulfate, soil dust, and sea salt,
420 and the precursor gases of sulfate, i.e., sulfur dioxide (SO₂) and dimethyl sulfide
421 (DMS). The aerosol transport processes include emission, advection, diffusion, sulfur
422 chemistry, wet deposition, dry deposition, and gravitational settling.

423 Although SPRINTARS was originally based on a general circulation model
424 (GCM), i.e., CCSR/NIES/FRCGC AGCM (Numaguti et al., 1997) called the Model
425 for Interdisciplinary Research on Climate (MIROC) to investigate the regional
426 distribution and transport of dust and anthropogenic aerosols over the TP, we
427 combined SPRINTARS with a regional-scale NHM developed by the Japan
428 Meteorological Agency (JMANHM) (Saito et al., 2006). The dynamical field of the
429 JMA-NHM drives the transport of aerosols included in SPRINTARS (hereafter
430 referred to as NHM-SPRINTARS or simply SPRINTARS).

431 The Arakawa-C and Lorentz grid structures were adopted for the horizontal and
432 vertical grid configurations, respectively. Originally, the advection scheme for tracers
433 (i.e., mixing ratio of hydrometeors, aerosols and gases) in NHM did not guarantee
434 mass conservation. In adding SPRINTARS to NHM in this study, the advection
435 scheme of Walcek and Aleksic (1998), which guarantees mass conservation, was
436 applied in the transport of aerosols and chemical tracers. Using the advection scheme,
437 Kajino et al. (2012) successfully simulated the transport of a chemical tracer. The

438 turbulence scheme of Nakanishi and Niino (2006) and the two-moment bulk cloud
439 microphysical scheme of Yamada (2003) were used.

440 **2.2 Experiment setup**

441 A simulation of the coupled NHM and SPRINTARS was conducted. The model
442 domain covered 15.72-53.33 °N and 60.58-119.09 °E, as shown in Fig. 1. A horizontal
443 resolution of 20km × 20km was used. Vertically, 40 levels with variable intervals
444 from 40 to 1120 m were used. The experiment was conducted for August of 2007 at a
445 time step of $\Delta t = 5.0$ s.

446 The 6 h dataset of Japanese 25 year Reanalysis (JRA-25) (Onogi et al., 2007)
447 was used for the initial and lateral boundaries of the horizontal wind field,
448 temperature, and specific humidity during the simulated period. The vertical wind
449 field of the initial and boundary conditions was set to 0.

450 The initial and boundary conditions of the aerosol fields were created through
451 downscaling the results of SPRINTARS in a general circulation model, MIROC-
452 SPRINTARS (Takemura et al., 2005; Goto et al., 2011). Every 6 h result from
453 MIROC-SPRINTARS, for which the horizontal and vertical resolutions were $1.1^\circ \times$
454 1.1° and 20 layers, respectively, was interpolated to determine the initial and lateral
455 boundary conditions of the aerosol and precursor gases (DMS and SO₂) (details on the
456 experiment setup of MIROC-SPRINTARS are described in the Appendix).

457 The emission inventory data of anthropogenic black carbon and SO₂ are based on
458 Lamarque et al. (2011), and the other inventories (i.e., biomass burning and volcanoes)
459 are the same as those used by Takemura et al. (2005). In addition to the aerosol field
460 and emission data, the three-dimensional oxidant distribution is required to calculate
461 the chemical reaction of sulfate aerosols in each grid. The monthly mean oxidant
462 distributions were prescribed from the chemical transport model CHASER coupled
463 with MIROC (MIROC-CHASER) (Sudo et al., 2002), with a horizontal resolution of
464 $2.8^\circ \times 2.8^\circ$.

465 The original pre-calculated parameters of simulated aerosols used in this study,

466 refractive indices at 0.55 μm and effective radius, are listed in Table 1. In this model,
467 the particle sizes of dust, BC, OC, sea salt and sulfate aerosols is divided into 10, 9, 9,
468 4 and 8 radii, respectively, for different radius ranges as given in Table 1. And the
469 refractive index of each aerosol component is uniform for all the radius subranges
470 based on d'Almeida et al. (1991) and the imaginary part of soil dust aerosols is
471 updated for their weaker absorption of the solar radiation (Kaufman et al., 2001).

472

473 **3 Observational data**

474 **3.1 CALIPSO profiles**

475 Combining an active Lidar instrument, i.e., the Cloud-Aerosol Lidar with Orthogonal
476 Polarization (CALIOP), with passive infrared and visible imagers, the CALIPSO
477 satellite provides new insight into the vertical structure and properties of clouds and
478 aerosols. In this study, the CALIPSO Level 1B and Level 2APro datasets (aerosol
479 profile), which contain a half-orbit (day or night) of calibrated and geolocated single-
480 shot (highest resolution) Lidar profiles, were used to detect dust events and evaluate
481 the model.

482 The CALIPSO Level 1B product provides the profiles of the total attenuated
483 backscatter at 532 and 1064 nm and a volume depolarization ratio at 532 nm; the
484 ~~column~~ optical depth of aerosols from CALIPSO Level 2APro was used to increase
485 the reliability of the dust detection. The Level 2APro product also provides the
486 extinction coefficient profiles at 532 nm, which were used to evaluate the
487 SPRINTARS model in the vertical direction. Because aerosols and clouds generally
488 have a larger spatial variability and stronger backscatter intensity at lower altitudes,
489 the investigation focuses on altitudes ranging from 0 to 10 km a.s.l. to obtain a higher
490 accuracy.

491 **3.2 OMI AI**

492 The ozone monitoring instrument (OMI) aboard the Earth Observation System (EOS)
493 Aura spacecraft provides daily global coverage of the Earth-atmosphere system at

494 wavelengths ranging from 270 to 500 nm with a high spatial resolution of 13 km × 24
495 km and a swath width of approximately 2600 km. The OMI Aerosol (OMAERO)
496 Level 2 product contains the characteristics of absorbing aerosols in the full
497 instrument resolution. The OMI AI in the UV band was compared with the aerosol
498 optical depth (AOD) simulated by SPRINTARS.

499 **3.3 MISR AOD**

500 The MISR, which was launched with the sun-synchronous polar-orbiting Terra, can
501 simultaneously view the sunlit Earth at the same point in nine widely spaced angles
502 ranging from 70 ° afterward to 70 ° forward of the local vertical at a spatial sampling
503 resolution of 275 to 1100 m globally. The MISR can even retrieve aerosol properties
504 over highly reflective surfaces, such as deserts, and it has few limitations caused by
505 the surface type (Christopher et al., 2008; Kahn et al., 2005; Martonchik, 2004). The
506 MISR Level 3 AOD product, which is retrieved from multiple orbits at a monthly time
507 scale on geographic grids of 0.5 ° × 0.5 °, was used to evaluate the simulated monthly
508 properties of all of the aerosols in this study.

509 **3.4 ERA-Interim reanalysis data**

510 The European Centre for Medium-Range Weather Forecasts (ECMWF) ERA-Interim
511 reanalysis dataset was used to evaluate the meteorological fields of SPRINTARS and
512 analyze the transport of the aerosols. Daily meteorological contours of the *U* and *V*
513 components of the wind speed and the vertical velocity from ECMWF were used. The
514 reanalysis data has a spatial resolution of 1.0 ° × 1.0 °, 37 pressure levels in the vertical
515 direction, and a temporal resolution of 6 h (00:00, 06:00, 12:00 and 18:00 UTC).

516

517 **4 Results and discussion**

518 Considering the influence of the lateral boundary of the model domain, the analysis
519 primarily focused on the inner domain of 20-50 °N, 70-110 °E, as indicated by the
520 black rectangle in Fig. 1; this area encloses the TP and most of the dust sources in
521 East Asia.

522 The TP is located in central East Asia (25-40 °N, 74-104 °E), where the average
523 elevation is 4500 m. ~~For the northeast TP~~~~Northeast of the TP~~, the Taklimakan,
524 Gurbantungut, Badain, and Jaran Deserts are the primary dust sources outside the
525 local desert in the Qaidam Basin. ~~For the west TP~~~~West of the TP~~, the Taklimakan
526 Desert, Great Indian Desert and deserts in Central Asia are the primary dust sources.
527 Although the area southeast of the TP is far from the dust sources, anthropogenic
528 aerosols could be transported from India and east of China. The aerosols over the TP
529 may consist of particles transported from these sources and anthropogenic aerosols,
530 including carbonaceous and sulfate aerosols from India and east of China. The solid
531 black line in Fig. 1 indicates the trajectory of the CALIPSO satellite over the TP on 22
532 August 2007.

533 **4.1 Identification of a dust event**

534 The product of CALIPSO, which can observe aerosols over bright surfaces and
535 beneath thin clouds in clear skies (Vaughan et al., 2004; Winker et al., 2006), was
536 used to identify dust aerosols. With a total attenuated backscatter coefficient at 532
537 nm, the depolarization ratio and ~~columnar~~-AOD from CALIPSO were combined to
538 identify dust aerosols. Generally, because of its non-sphericity, dust has a larger
539 depolarization ratio than ~~raindrops~~~~rain~~~~clouds~~ and other aerosols and has a smaller
540 depolarization ratio than an ice cloud. To identify dust aerosols, values of 0.0008-
541 $0.048 \text{ km}^{-1} \text{ sr}^{-1}$ and 0.06-0.4 were chosen as the thresholds of the total attenuated
542 backscatter and volume depolarization ratio, respectively (Chen et al., 2009; Li et al.,
543 2013; Liu et al., 2008; Shen et al., 2010; Zhao et al., 2009).

544 The CALIPSO data analysis shows (figures omitted) that a large amount of
545 aerosols are present over the TP during summer. A typical case on 22 August 2007
546 was investigated in detail. Figure 2 shows the (a) ~~columnar~~-AOD, the altitude-orbit
547 cross-section of the (b) total attenuated backscattering intensity and (c) depolarization
548 ratio on 22 August 2007 along the CALIPSO trajectory presented in Fig. 1. The gray
549 shading in Fig. 2 indicates the topography, and the deep blue area denotes the absence
550 of a signal due to clouds, which the laser cannot penetrate. As shown in Fig. 2, the

551 total attenuated backscatter and volume depolarization ratio ranged from 0.002 to
552 $0.005 \text{ km}^{-1} \text{ sr}^{-1}$ and 0.06 to 0.3, respectively. Based on the thresholds for identifying
553 dust aerosols, 22 August 2007 is considered a severe dusty day. Thick dust plumes
554 existed over both the southern and northern slopes of the TP (Fig. 2b and c). Figure 2a
555 presents the ~~columnar~~-AOD on 22 August 2007 over the TP. The large AOD values
556 further verify the conclusion from the total attenuated backscatter and volume
557 depolarization ratio. The dust plumes could extend up to approximately 7-8 km a.s.l.
558 over the northern slope of the TP. The result also indicates that the dust plumes over
559 the northern slope were much thicker than those over the southern slope of the TP.

560 Based on the dust event detected by the CALIPSO observations, the model
561 simulation and relative analysis were performed in the following sections.

562 **4.2 Simulation and comparison with observations**

563 Considering the geographical features of the TP, we primarily investigated the
564 simulation_s of dust, carbonaceous aerosols (organic and black carbon), and sulfate
565 aerosols. The simulated optical depths of the dust and the carbonaceous and sulfate
566 aerosols from 21 August 00:00 UTC to 24 August 00:00 UTC are shown in Fig. 3b
567 and c. The OMI AI in the UV band, which can detect UV-absorbing aerosols, is
568 shown in Fig. 3a. The AI from the OMI is gridded at $0.5^\circ \times 0.5^\circ$ from the satellite orbit
569 files. Generally, the value of the AI ranges from -1.5 to 3.5, in which negative and
570 positive indicate the dominance of scattering (e.g., sulfate) and absorbing aerosols
571 (e.g., black carbon and dust) (Christopher et al., 2008), respectively.

572 The OMI satellite observed a large amount of UV-absorbing aerosols around the
573 Taklimakan Desert and Inner Mongolia and north of the TP, as shown in Fig. 3a.
574 Although many invalid values exist in the OMI observational data, the AI suggests
575 highly absorbing aerosols around the Taklimakan Desert, the southern slope and the
576 area east of the TP. The highest AI value was greater than 3.5 on 23 August.
577 Additionally, compared with the OMI observation, SPRINTARS observed similar
578 AOD patterns over the northern slope (Fig. 3b), the southern slope and the east of the
579 TP (Fig. 3c). The model simulation indicates that dust aerosols were primarily

580 distributed over the northern slope of the TP, whereas anthropogenic aerosols,
581 including carbonaceous and sulfate aerosols, were distributed over the southern slope
582 and east of the TP. Combining the observations from the OMI and the SPRINTARS
583 | simulations, the absorbing aerosols over the north TP slope were dust, and those over
584 the southern slope and east of the TP were carbonaceous materials.

585 Figure 4 shows the simulated distributions of the column-integrated aerosol
586 single scattering albedo (SSA) and Angstrom exponent (AE) for a mixed
587 polydispersion of all aerosols in this study. The black rectangles indicate the key areas
588 where the values clearly change. In addition to the low SSA values over much of the
589 snow cover, the SSA values around the Taklimakan Desert were as low as 0.85-0.91
590 because of the strong absorption of direct solar radiation. From 21 to 23 August, the
591 low SSA center clearly moved from the Taklimakan Desert to the northern slope and
592 east part of the TP (shown in the solid boxes in Fig. 4). The decreasing SSA and AE
593 | ~~over the northern slope of the TP~~ imply increasing absorption and larger particles ~~over~~
594 | ~~the northern slope~~. As the dashed boxes indicate, over the southern slope of the TP,
595 the SSA ranged from 0.88 to 0.91 and exhibited a decrease from 21 to 23 August. At
596 the same time, to the east of the TP, the SSA values varied from approximately 0.85
597 to 0.98 while the AE values somewhat decreased from 21 to 23 August (dotted boxes).
598 | The simulations suggest that the eastward and southward migration of dust aerosols
599 | induced the increasing SSA over the northern slope and east of the TP,
600 | respectively~~The simulation suggests that the eastward and southward migration of~~
601 | ~~dust aerosols induced the declining SSA over the northern slope and east of the TP;~~
602 however, the carbonaceous aerosols contributed to the SSA variation over the
603 southern slope of the TP. Additionally, east of the TP, the sulfate aerosols somewhat
604 influenced the simulated SSA and AE values.

605 Although the satellite observations were compared with the horizontal
606 distribution of aerosols over and around the TP, in situ vertical observations are
607 difficult to find due to the special geographical environment. Considering the
608 limitation of the spatial and temporal coverage due to aerosol-property retrievals over

609 bright surfaces and beneath thin clouds, we compared the CALIPSO observations
610 with the simulated vertical distribution along the orbit of CALIPSO/CALIOP at 20:18
611 UTC on 22 August 2007. Figure 5 presents the extinction coefficient of the CALIPSO
612 retrieval and the model simulation along the orbit path (as shown in Fig. 1). Although
613 a slight underestimation occurs in the SPRINTARS simulation, the comparison shows
614 that the model can nearly reasonably simulate the aerosol extinction profiles over
615 most of the orbit paths. Both the CALIPSO retrieval and SPRINTARS simulation
616 show high aerosol loading around the Taklimakan Desert (38-41 °N) and the Tulufan
617 Basin (approximately 43 °N). Based on the satellite observations and model
618 simulations, aerosols over the Taklimakan Desert ascended over the TP, passing the
619 northern slope, to 7-8 km a.s.l. (33-39 °N). Except for the underestimation of the
620 extinction coefficient over the southern slope of the TP, the spatial patterns of the
621 extinction coefficient between the observations and simulations agree well.

622 Considering the missing observations of MISR, we compared the simulated
623 monthly aerosol optical properties with the satellite observations on August 2007 over
624 the TP.~~Considering the missing satellite observations over 21-23 August, we~~
625 ~~compared the simulated monthly aerosol optical properties with the MISR~~
626 ~~observations on August 2007 over the TP.~~ Figure 6 compares the monthly AOD
627 between the MISR observations (Fig. 6d), which are used in addition to the OMI, and
628 the SPRINTARS simulations. Figure 6a and b describe the distributions of the AOD
629 for dust and anthropogenic (carbonaceous and sulfate) aerosols, and the total AOD of
630 four types of aerosols (dust, sulfate, sea salt, and carbonaceous aerosols) is
631 represented in Fig. 6c. A comparison between Fig. 6c and d shows that SPRINTARS
632 can simulate the pattern and magnitude of the AOD extremely well. During August
633 2007, the monthly mean AOD reached over 1.5 around the Taklimakan Desert and the
634 Sichuan Basin. The high optical depths around the Taklimakan Desert were primarily
635 due to dust aerosols; however, the high values around the Sichuan Basin were
636 primarily due to anthropogenic aerosols.

637 As suggested in Figs. 3 and 6, SPRINTARS can successfully simulate the

638 distribution of dust and anthropogenic aerosols. The transport of the dust and
639 anthropogenic aerosols to the TP is described in the following section.

640 **4.3 Transport of aerosols over the TP**

641 As indicated in the simulation of SPRINTARS over the TP area, dust particles are
642 primarily distributed around deserts, such as the Taklimakan Desert, whereas
643 carbonaceous and sulfate aerosols are primarily distributed in the northern India
644 Peninsula and east of the TP. The transport of dust and anthropogenic aerosols over
645 the TP from 21 to 23 August is further investigated.

646 Combining the distribution of the aerosol optical properties shown in Figs. 3 and
647 4, the high aerosol mass over the northern slope of the TP is attributed to dust,
648 whereas the dominant aerosol type over the southern slope and east of the TP is
649 anthropogenic. The dust aerosols over the northern slope of the TP predominately
650 originate from the neighboring Taklimakan~~Taklamakan~~ Desert. Near the southern
651 slope of the TP, the anthropogenic aerosols in the east primarily originate from India,
652 and the dust in the west primarily originates from the Great Indian Desert. East of the
653 TP, the dust particles primarily come from the Taklimakan~~Taklamakan~~ Desert and
654 from local dust sources, whereas anthropogenic aerosols originate from eastern China.
655 The aerosols mobilized from the above sources are further transported to the TP
656 during favorable meteorological conditions. Figure 7 presents the wind fields at the
657 850 hPa level from ERA-Interim (a) and the fields at $z = 20$ m from SPRINTARS (b)
658 during 21-23 August. The wind fields of SPRINTARS were averaged to the horizontal
659 resolution of the ERA-Interim data ($1.0^\circ \times 1.0^\circ$). In Fig. 7b, the arrows denote the U
660 and V wind components in the horizontal direction, and the color indicates the vertical
661 wind velocity, in which a positive value is a downdraft and a negative value is an
662 updraft. Again, the comparison between the simulated fields and the observed fields
663 proves the reliability of the SPRINTARS simulation. Comparing the vertical wind
664 velocity over the southern slope, the updraft appears stronger over the northern slope
665 of the TP.

666 The wind near the surface blows from Kazakhstan to the Tianshan and Altai

667 Mountains, in which a northwesterly current continuously moves to the east, whereas
668 another current turns into northeasterly wind toward the TP~~whereas another current~~
669 ~~curves northeast~~ because of topographic blocking. Figure 7 suggests that with the
670 northwesterly wind current, dust particles are transported to the east of the TP. At the
671 same time, a large amount of dust is transported to the northern slope of the TP as
672 northeasterly winds form. From 21 to 23 August, the northeasterly wind from the
673 Tianshan and Altai Mountains was strongest on 22 August and weakened on 23
674 August. Furthermore, except for the northeasterly airflow toward the TP, an eastward
675 airflow branched off of the northwesterly current, which apparently increased on 22
676 August. This airflow can transport dust that originated from the Taklimakan Desert to
677 the eastern TP, as shown in Fig. 7. The movement of dust from the Taklimakan Desert
678 to the east induces variations in the SSA and AE distributions, as shown in Fig. 4.

679 Additionally, Fig. 7 shows strong southwesterly wind from India. As shown in
680 Fig. 7a1 and b1, the strong cyclone over the India Peninsula induced a northward
681 transport of anthropogenic aerosols. According to Figs. 3 and 6, anthropogenic
682 aerosols are transported to the southern TP during southwesterly winds from the India
683 Peninsula. As the southwesterly wind weakens, the amount of transported
684 anthropogenic particles declines, as shown in Fig. 3c3. Simultaneously, the
685 anthropogenic aerosols from eastern China are transported to the eastern TP with
686 easterly wind~~a westerly wind~~.

687 To determine the transport of aerosols in the horizontal and vertical directions,
688 we analyzed the vertical variation in the dust aerosol mass concentration in the west-
689 to-east and south-to-north directions at 37°N and 78°E, respectively, as shown in Fig.
690 8. The cross-sections cut across the center of the high AOD area for dust aerosols, as
691 shown in Fig. 3b, to explore the dust transport from 21 to 23 August 2007. As the
692 easterly wind weakened and the northwesterly wind strengthened over the area from
693 22 to 23 August, dust aerosols were continuously transported eastward, as indicated
694 by the increasing SSA in Fig. 4a2 and a3. As suggested in Fig. 8a1 and b1, on 21
695 August, the dust storm began to outbreak~~at dust particles arrived at~~ approximately

696 78 °E, 37 °N and extended up to approximately 8 km. Dust mobilization became more
697 active and expansive the following day. With the development and transportation of
698 the dust particles in the following two days, the particles were transported to higher
699 and even upward to 9 km (Fig. 8a3 and 8b3). ~~On 22 August, the dust was transported~~
700 ~~upward to 9 km, and the aerosol mass concentration around the outbreak location~~
701 ~~weakened (Fig. 8a2).~~ Simultaneously, the dust aerosols were substantially transported
702 eastward ~~during 70-80 °E~~ ~~from 70 to 80 °E~~ on 22 August, when the wind field favored
703 eastward transport (Fig. 8a2). However, as shown in Fig. 8b2 and b3, most
704 southward-transported dust particles were blocked and lifted up to the TP due to the
705 orographic lifting. Based on Fig. 8b, a large updraft existed near the northern and
706 southern slopes of the TP that lifted the dust to the plateau. The aerosol mass
707 concentration was high in the west-east direction on 21 August and then strengthened
708 over the following two days. The southward-transported particles accumulated over
709 the northern slope of the TP, peaked on 23. Figure 8 further proves that the dust over
710 the northern slope of the TP originated from the deserts, primarily the Taklimakan
711 Desert. Combining Fig. 3c and the wind field in Fig. 7, we conclude that a large
712 amount of anthropogenic aerosols were transported to the area east of the TP during
713 the dust event and then weakened with the eastward transport of dust when the
714 eastward airflow strengthened.

715 Corresponding to the transport of dust aerosols in the horizontal and vertical
716 directions, Fig. 9 shows the distribution of dust mass column loading from 21 to 23
717 August. As suggested in Fig. 9, the dust loading is high over the northern and
718 southern slopes of the TP. With the development and transportation, dust mass
719 concentration over the northern slope began to increase and extend southeastward on
720 21 August. ~~The aerosol mass concentration began to increase and extend~~
721 ~~southeastward on 21 August.~~ On the following two day, 22-23 August, the dust event
722 became severe and swept across the entire Tarim Basin. With the formation of the
723 dust event on 21 August, the northeasterly wind over the northeastern TP was strong,
724 and a large amount of carbonaceous aerosols was transported to eastern TP; this setup

725 produced a high AOD and low SSA values, as shown in Figs. 3c1 and 4a1,
726 respectively.

727

728 **5 Conclusion**

729 In this study, we first evaluated the SPRINTARS model coupled with a NHM using
730 CALIPSO, OMI and MISR observational data. Simultaneously, the summer dust and
731 anthropogenic aerosols over the TP were evaluated, and the distributions over the TP
732 were presented.

733 From the SPRINTARS simulation_s, dust aerosols contribute to the high AOD
734 around the Taklimakan Desert, and the absorbing aerosols, mainly carbon, observed
735 by the OMI satellite were distributed over the southern TP. SPRINTARS can simulate
736 an AOD pattern similar to that observed by the OMI, with the exception of several
737 high values east of the TP. Additionally, the model simulation_s suggests that
738 anthropogenic aerosols, i.e., carbonaceous and sulfate aerosols, surround India and the
739 Sichuan Basin. Compared with the vertical distribution of the aerosol extinction
740 coefficient along the orbit of CALIPSO/CALIOP, SPRINTARS can reasonably
741 simulate the aerosol extinction profiles over most of the orbits. SPRINTARS well
742 simulated the pattern and magnitude of the monthly aerosol optical properties
743 observed by the MISR on August 2007 over the TP. The aerosols were primarily
744 anthropogenic particles in the east and southern slope of the TP but are dust particles
745 over the northern slope of the TP.

746 The vertical-longitude/latitude cross-sections of the SPRINTARS-simulated
747 aerosol mass concentration show that the dust aerosols were emitted in the
748 atmosphere at approximately 78 °E, 37 °N and extended up to approximately 8 km
749 from the first day of the dust event. Then, the dust was transported upward to 9 km;
750 simultaneously, the dust aerosols were substantially transported east the following day.
751 During the southward transport, the dust particles were blocked and lifted up to the TP
752 due to the orographic lifting of the plateau. As the dust event weakened, the transport

753 weakened in both the vertical and horizontal directions. During the dust events, the
754 model simulations showed that the Tibetan dust aerosols appear at approximately 7-8
755 km a.s.l., and the plumes originated from the nearby Taklimakan Desert and
756 accumulated over the northern slopes of the TP during the summer.

757 The dust aerosols were transported eastward by strong northwesterly winds,
758 whereas the dust was transported southward to the northern slope of the TP as the air
759 current changed from northwesterly to northeasterly due to topographic blocking.
760 Additionally, increasingly eastward airflow branched off from the northwesterly wind
761 to transport a portion of the dust aerosols to eastern China. Anthropogenic aerosols
762 that originate from eastern China are transported to the east of the TP. Influenced by
763 the Indian summer monsoon, anthropogenic aerosols are northwardly transported to
764 the southern slope of the TP.

765 The impact of different aerosols on cloud properties and precipitation is an
766 important issue. In the future, the interaction of dust and anthropogenic aerosols with
767 the microphysical properties of clouds will be further investigated.

768

769

770

771

772

773

774

775

776

777

778

779

780

781 **Appendix: Details of the MIROC-SPRINTARS data used for the initial and**
782 **boundary conditions of the aerosol field of NHM-SPRINTARS**

783 To create the initial and boundary conditions of the aerosol fields for NHM-

784 SPRINTARS, we used the results of MIROC-SPRINTARS (Takemura et al., 2005;

785 Goto et al., 2011). MIROC-SPRINTARS was based on the 6 hourly meteorological

786 fields (temperature, winds, and water vapor) of NCAR/NCEP Reanalysis. The results

787 of the calculation were used for the initial and boundary conditions in this study. The

788 horizontal and vertical resolutions were set to $1.1^{\circ} \times 1.1^{\circ}$ and 20 layers, respectively.

789 The emission inventories of anthropogenic black carbon (BC) and sulfur dioxide (SO₂)

790 were generated by Streets et al. (2003) over Asia and by Takemura et al. (2005) over

791 the remaining regions. The other inventories (biomass burning and volcanoes) were

792 the same as those used in Takemura et al. (2005). In MIROC-SPRINTARS, the

793 monthly mean oxidant distributions were prescribed from a global chemical transport

794 model, MIROC-CHASER (Sudo et al., 2002), with a horizontal resolution of $2.8^{\circ} \times$

795 2.8° .

796

797

798

799

800

801

802

803

804

805

806

807

808

809

810

811 *Author contributions:* Y. Liu and Y. Sato contributed equally to this work.

812

813

814 *Acknowledgements.* This research was jointly supported by the National Basic
815 Research Program of China (2012CB955301), the National Natural Science
816 Foundation of China (41475095 and 41275006), the Fundamental Research Funds for
817 the Central Universities (lzujbky-2015-ct03, lzujbky-2014-109, and lzujbky-2009-
818 k03), and the China 111 project (B13045). Part of this research was supported by
819 funds from MOEJ/S12&GOSAT2, JST/CREST/TEEDDA,
820 JAXA/EarthCARE&GCOM-C. The CALIPSO data were obtained from the National
821 Aeronautics and Space Administration (NASA) Langley Research Center
822 Atmospheric Sciences Data Center. The ERA-Interim data were provided by the
823 European Centre for Medium Range Weather Forecasts
824 (<http://apps.ecmwf.int/datasets/>). The OMI and MISR data were provided by NASA
825 (ftp://aurapar2u.ecs.nasa.gov/data/s4pa/Aura_OMI_Level2/OMAERO.003/ and
826 https://eosweb.larc.nasa.gov/project/misr/mil3dae_table). The authors are extremely
827 grateful to Takemura of Kyushu University and Goto of the National Institute for
828 Environmental Research on Japan for developing and maintaining SPRINTARS. The
829 authors are also thankful to Kajino of Meteorological Research Institute for his
830 supplying code of advection scheme.

831

832

833

834

835

836

837

838

839

840

References

841 Breider, T. J., Mickley, L. J., Jacob, D. J., Wang, Q., Fisher, J. A., Chang, R. Y. W., and Alexander, B.:
842 Annual distributions and sources of Arctic aerosol components, aerosol optical depth, and aerosol
843 absorption, *J. Geophys. Res.-Atmos.*, 119, 4107-4124, doi:10.1002/2013JD020996, 2014.

844 Chen, S., Huang, J., Zhao, C., Qian, Y., Leung, L. R., and Yang, B.: Modeling the transport and
845 radiative forcing of taklimakan dust over the tibetan plateau: a case study in the summer of 2006,
846 *J. Geophys. Res.-Atmos.*, 118, 797-812, doi:10.1002/jgrd.50122, 2013.

847 Chen, Y., Mao, X., Huang, J., Zhang, H., Tang, Q., Pan, H., and Wang, C.: Vertical distribution
848 characteristics of aerosol during a long-distance transport of heavy dust pollution, *China Environ.*
849 *Sci.*, 29, 449-454, 2009.

850 Christopher, S. A., Gupta, P., Haywood, J., and Greed, G.: Aerosol optical thicknesses over North
851 Africa: 1. Development of a product for model validation using Ozone Monitoring Instrument,
852 Multiangle Imaging Spectroradiometer, and Aerosol Robotic Network, *J. Geophys. Res.-Atmos.*,
853 113, D00C04, doi:10.1029/2007JD009446, 2008.

854 d'Almeida, G. A., Koepke, P., and Shettle, E. P.: *Atmospheric Aerosols: Global Climatology and*
855 *Radiative Characteristics*, A. Deepak, Hampton, Va, 561, 1991.

856 DeMott, P. J., Sassen, K., Poellot, M. R., Baumgardner, D., Rogers, D. C., Brooks, S. D., Prenni, A. J.,
857 and Kreidenweis, S. M.: African dust aerosols as atmospheric ice nuclei, *Geophys. Res. Lett.*, 30,
858 1732, doi:10.1029/2003GL017410, 2003.

859 Gong, S. L., Zhang, X. Y., Zhao, T. L., Zhang, X. B., Barrie, L. A., McKendry, I. G., and Zhao, C. S.: A
860 Simulated climatology of Asian dust aerosol and its trans-Pacific transport. Part II: Interannual
861 variability and climate connections, *J. Climate*, 19, 104-122, doi:10.1175/JCLI3606.1, 2006.

862 Goto, D., Nakajima, T., Takemura, T., and Sudo, K.: A study of uncertainties in the sulfate distribution
863 and its radiative forcing associated with sulfur chemistry in a global aerosol model, *Atmos. Chem.*
864 *Phys.*, 11, 10889-10910, doi:10.5194/acp-11-10889-2011, 2011.

865 Goudie, A. S. and Middleton, N. J.: Saharan dust storms: nature and consequences, *Earth-sci. Rev.*, 56,
866 179-204, doi:10.1016/S0012-8252(01)00067-8, 2001.

867 Hansen, J., Sato, M., Ruedy, R., Lacis, A., and Oinas, V.: Global warming in the twenty-first century:
868 an alternative scenario, *P. Natl. Acad. Sci. USA*, 97, 9875-9880, doi:10.1073/pnas.170278997,
869 2000.

870 Hsu, S. C., Tsai, F., Lin, F. J., Chen, W. N., Shiah, F. K., Huang, J. C., Chan, C. Y., Chen, C. C., Liu, T.
871 H., Chen, H. Y., Tseng, C. M., Hung, G. W., Huang, C. H., Lin, S. H., and Huang, Y. T.: A super
872 Asian dust storm over the East and South China Seas: disproportionate dust deposition, *J.*
873 *Geophys. Res.-Atmos.*, 118, 7169-7181, doi:10.1002/jgrd.50405, 2013.

874 [Huang, J., Fu, Q., Zhang, W., Wang, X., Zhang, R., Ye, H., and Warren, S.: Dust and black carbon in](#)

875 [seasonal snow across northern China, B. Am. Meteorol. Soc., 92 \(2\), 175-181,](#)
876 [doi:10.1175/2010BAMS3064.1, 2011.](#)

877 [Huang, J., Ge, J., and Weng, F.: Detection of Asia dust storms using multisensor satellite](#)
878 [measurements, Remote Sens. Environ., 110\(2\), 186-191, 2007a.](#)

879 [Huang, J., Minnis, P., Yan, H., Yi, Y., Chen, B., Zhang, L., and Ayers, J. K.: Dust aerosol effect on](#)
880 [semi-arid climate over Northwest China detected from A-Train satellite measurements, Atmos.](#)
881 [Chem. Phys., 10, 6863-6872, doi:10.5194/acp-10-6863-2010, 2010.](#)

882 Huang, J., Minnis, P., Yi, Y., Tang, Q., Wang, X., Hu, Y., Liu, Z., Ayers, K., Trepte, C., and Winker, D.:
883 Summer dust aerosols detected from CALIPSO over the Tibetan Plateau, Geophys. Res. Lett., 34,
884 L18805, doi:10.1029/2007gl029938, 2007b.

885 ~~Huang, J., Minnis, P., Yan, H., Yi, Y., Chen, B., Zhang, L., and Ayers, J. K.: Dust aerosol effect on~~
886 ~~semi-arid climate over Northwest China detected from A-Train satellite measurements, Atmos.~~
887 ~~Chem. Phys., 10, 6863-6872, doi:10.5194/acp-10-6863-2010, 2010.~~

888 Huang, J., Minnis, P., Yan, H., Yi, Y., Chen, B., Zhang, L., and Ayers, J. K.: Dust aerosol effect on
889 semi-arid climate over Northwest China detected from A-Train satellite measurements, Atmos.
890 Chem. Phys., 10, 6863-6872, doi:10.5194/acp-10-6863-2010, 2010.

891 Jacobson, M. Z.: Strong radiative heating due to the mixing state of black carbon in atmospheric
892 aerosols, Nature, 409, 695-697, doi:10.1038/35055518, 2001.

893 Kahn, R. A., Gaitley, B. J., Martonchik, J. V., Diner, D. J., and Crean, K. A.: Multiangle Imaging
894 Spectroradiometer (MISR) global aerosol optical depth validation based on 2 years of coincident
895 Aerosol Robotic Network (AERONET) observations, J. Geophys. Res.-Atmos., 110, D10S04, doi:
896 10.1029/2004jd004706, 2005.

897 Kajino, M., Inomata, Y., Sato, K., Ueda, H., Han, Z., An, J., Katata, G., Deushi, M., Maki, T., Oshima,
898 N., Kurokawa, J., Ohara, T., Takami, A., and Hatakeyama, S.: Development of the RAQM2
899 aerosol chemical transport model and predictions of the Northeast Asian aerosol mass, size,
900 chemistry, and mixing type, Atmos. Chem. Phys., 12, 11833-11856, doi:10.5194/acp-12-11833-
901 2012, 2012.

902 Kaufman, Y. J., Tanré, D., Dobocik, O., Karnieli, A., and Remer, L. A.: Absorption of sunlight
903 by dust as inferred from satellite and groundbased remote sensing, Geophys. Res. Lett., 28,
904 1479-1482, 2001.

905 Lamarque, J.-F., Bond, T. C., Eyring, V., Granier, C., Heil, A., Klimont, Z., Lee, D., Liousse, C.,
906 Mieville, A., Owen, B., Schultz, M. G., Shindell, D., Smith, S. J., Stehfest, E., Van Aardenne, J.,
907 Cooper, O. R., Kainuma, M., Mahowald, N., McConnell, J. R., Naik, V., Riahi, K.,
908 and van Vuuren, D. P.: Historical (1850-2000) gridded anthropogenic and biomass burning
909 emissions of reactive gases and aerosols: methodology and application, Atmos. Chem. Phys., 10,
910 7017-7039, doi:10.5194/acp-10-7017-2010, 2010.

911 Lau, K. M. and Kim, K. M.: Observational relationships between aerosol and Asian monsoon rainfall,
912 and circulation, Geophys. Res. Lett., 33, L21814, doi:10.1029/2006gl027546, 2006.

913 Lau, K. M., Kim, M. K., and Kim, K. M.: Asian summer monsoon anomalies induced by aerosol direct
914 forcing: the role of the Tibetan Plateau, Clim. Dynam., 26, 855-864, doi:10.1007/s00382-006-

915 0114-z, 2006.

916 Li, H., Zheng, W., and Gong, Q.: An analysis on detection of a sand-dust weather over Taklimakan
917 Desert based on polarization micro-pulse lidar, *Desert Oasis Meteorol.*, 7, 1-5, 2013.

918 Liu, Y., Huang, J., Shi, G., Takamura, T., Khatri, P., Bi, J., Shi, J., Wang, T., Wang, X., and Zhang, B.:
919 Aerosol optical properties and radiative effect determined from sky-radiometer over Loess Plateau
920 of Northwest China, *Atmos. Chem. Phys.*, 11, 11455-11463, doi:10.5194/acp-11-11455-2011,
921 2011.

922 Liu Y., Shi, G., and Xie, Y.: Impact of dust aerosol on glacial-interglacial climate, *Adv. Atmos. Sci.*, 30,
923 1725-1731, doi:10.1007/s00376-013-2289-7, 2013.

924 Liu Y., Jia, R., Dai, T., and Shi, G.: A review of aerosol optical properties and radiative effects, *J.*
925 *Meteor. Res.*, 28, 1003-1028, doi:10.1007/s13351-014-4045-z, 2014.

926 Liu, Z., Liu, D., Huang, J., Vaughan, M., Uno, I., Sugimoto, N., Kittaka, C., Trepte, C., Wang, Z.,
927 Hostetler, C., and Winker, D.: Airborne dust distributions over the Tibetan Plateau and
928 surrounding areas derived from the first year of CALIPSO lidar observations, *Atmos. Chem.*
929 *Phys.*, 8, 5045-5060, doi:10.5194/acp-8-5045-2008, 2008.

930 Martonchik, J. V.: Comparison of MISR and AERONET aerosol optical depths over desert sites,
931 *Geophys. Res. Lett.*, 31, L16102, doi:10.1029/2004gl019807, 2004.

932 Miller, R. L. and Tegen, I.: Climate response to soil dust aerosols, *J. Climate*, 11, 3247-3267,
933 doi:10.1175/1520-0442(1998)011<3247:CRTSDA>2.0.CO;2, 1998.

934 Müller, D., Franke, K., Ansmann, A., Althausen, D., and Wagner, F.: Indo-Asian pollution during
935 INDOEX: microphysical particle properties and single-scattering albedo inferred from
936 multiwavelength lidar observations, *J. Geophys. Res.-Atmos.*, 108, 4600,
937 doi:10.1029/2003jd003538, 2003.

938 Nakajima, T., Sekiguchi, M., Takemura, T., Uno, I., Higurashi, A., Kim, D., Sohn, B. J., Oh, S. N.,
939 Nakajima, T. Y., Ohta, S., Okada, I., Takamura, T., and Kawamoto, K.: Significance of direct and
940 indirect radiative forcings of aerosols in the East China Sea region, *J. Geophys. Res.-Atmos.*, 108,
941 8658, doi:10.1029/2002JD003261, 2003.

942 Nakanishi, M. and Niino, H.: An improved Mellor-Yamada level-3 model: its numerical stability and
943 application to a regional prediction of advection fog, *Bound.-Lay. Meteorol.*, 119, 397-407, 2006.

944 Numaguti, A., Takahashi, M., Nakajima, T., and Sumi, A.: Description of CCSR/NIES atmospheric
945 general circulation model. Study on the climate system and mass transport by a climate model,
946 CGER's Supercomputer Monograph Report, 3, 1-48, Center for Global Environmental Research,
947 National Institute for Environmental Studies, Tsukuba, Japan, 1997.

948 Onogi, K., Tsutsui, J., Koide, H., Sakamoto, M., Kobayashi, S., Hatsushika, H., Matsumoto, T.,
949 Kadokura, S., Wada, K., Kato, K., Oyama, R., Ose, T., Mannoji, N., and Taira, R.: The JRA-25
950 reanalysis, *J. Meteorol. Soc. Jpn.*, 85, 369-432, doi:10.2151/jmsj.85.369, 2007.

951 Saito, K., Fujita, T., Yamada, Y., Ishida, J., Kumagai, Y., Anranami, K., Ohmori, S., Nagasawa, R., and
952 Kumagai, S.: The Operational JMA Nonhydrostatic Mesoscale model, *Mon. Weather Rev.*, 134,
953 1266-1298, doi:10.1175/mwr3120.1, 2006.

- 954 Shen, L., Sheng, L. and Chen, J.: Preliminary analysis of the spatial distribution of the dust aerosol in a
955 heavy dust storm, *J. Desert Res.*, 30, 1483-1490, 2010.
- 956 Sokolik, I. N. and Toon, O. B.: Direct radiative forcing by anthropogenic airborne mineral aerosols,
957 *Nature*, 381, 681-683, doi:10.1038/381681a0, 1996.
- 958 Streets, D. G., Bond, T. C., Carmichael, G. R., Fernandes, S. D., Fu, Q., He, D., Klimont, Z., Nelson, S.
959 M., Tsai, N. Y., Wang, M. Q., Woo, J.-H., and Yarber, K. F.: An inventory of gaseous and primary
960 aerosol emissions in Asia in the year 2000, *J. Geophys. Res.-Atmos.*, 108, 8809,
961 doi:10.1029/2002JD003093, 2003.
- 962 [Su, J., Huang, J., Fu, Q., Minnis, P., Ge, J., and Bi, J.: Estimation of Asian dust aerosol effect on cloud
963 radiation forcing using Fu-Liou radiative model and CERES measurements, *Atmos. Chem. Phys.*,
964 *8\(10\)*, 2763-2771, 2008.](#)
- 965 Sudo, K, Takahashi, M., Kurokawa, J.-I., and Akimoto, H.: CHASER: a global chemical model of the
966 troposphere 1. Model description, *J. Geophys. Res.-Atmos.*, 107, 4339,
967 doi:10.1029/2001JD001113, 2002.
- 968 Takemura, T., Okamoto, H., Maruyama, Y., Numaguti, A., Higurashi, A., and Nakajima, T.:
969 Global three-dimensional simulation of aerosol optical thickness distribution of various origins, *J.*
970 *Geophys. Res.-Atmos.*, 105, 17853-17873, doi:10.1029/2000jd900265, 2000.
- 971 Takemura, T., Uno, I., Nakajima, T., Higurashi, A., and Sano, I.: Modeling study of long-range
972 transport of Asian dust and anthropogenic aerosols from East Asia, *Geophys. Res. Lett.*, 29,
973 2158, doi:10.1029/2002GL016251, 2002.
- 974 Takemura, T., Nozawa, T., Emori, S., Nakajima, T. Y., and Nakajima, T.: Simulation of climate
975 response to aerosol direct and indirect effects with aerosol transport-radiation model, *J. Geophys.*
976 *Res.-Atmos.*, 110, D02202, doi:10.1029/2004JD005029, 2005.
- 977 Tegen, I.: Modeling the mineral dust aerosol cycle in the climate system, *Quaternary Sci. Rev.*,
978 22, 1821-1834, doi:10.1016/s0277-3791(03)00163-x, 2003.
- 979 Thulasiraman, S., O'Neill, N. T., Royer, A., Holben, B. N., Westphal, D. L., and McArthur, L. J. B.:
980 Sunphotometric observations of the 2001 Asian dust storm over Canada and the U.S., *Geophys.*
981 *Res. Lett.*, 29, 96-1-96-4, doi:10.1029/2001GL014188, 2002.
- 982 Uno, I., Amano, H., Emori, S., Kinoshita, K., Matsui, I., and Sugimoto, N.: Trans-Pacific yellow
983 sand transport observed in April 1998: a numerical simulation, *J. Geophys. Res.-Atmos.*,
984 106, 18331-18344, doi:10.1029/2000JD900748, 2001.
- 985 Vaughan, M. A., Young, S. A., Winker, D. M., Powell, K. A., Omar, A. H., Liu, Z., Hu, Y., and
986 Hostetler, C. A.: Fully automated analysis of space-based lidar data: an overview of the CALIPSO
987 retrieval algorithms and data products, *Laser Radar Tech. Atmos. Sens.*, 5575,
988 16-30, doi:10.1117/12.572024, 2004.
- 989 Walcek, C. J. and Aleksic, N. M.: A simple but accurate mass conservative, peak-preserving,
990 mixing ratio bounded advection algorithm with fortran code, *Atmos. Environ.*, 32, 3863-3880,
991 doi:10.1016/S1352-2310(98)00099-5, 1998.
- 992 Winker, D., Vaughan, M., and Hunt, B.: The CALIPSO mission and initial results from CALIOP,

993 Proc. SPIE, 6409, 604902, doi:10.1117/12.698003, 2006.

994 Wu, G., Liu, Y., Zhang, Q., Duan, A., Wang, T., Wan, R., Liu, X., Li, W., Wang, Z., and Liang, X.:
995 The influence of mechanical and thermal forcing by the Tibetan Plateau on Asianl Climate,
996 J. Hydrometeorol., 8, 770–789, doi:10.1175/jhm609.1, 2007.

997 Yamada, Y.: Cloud microphysics, in: The JMA Nonhydrostatic Model, Annu. Rep., Jpn. Meteorol.
998 Agency, 49, 52-76, 2003 (in Japanese).

999 Zhang, X. Y., Arimoto, R., Cao, J. J., An, Z. S., and Wang, D.: Atmospheric dust aerosol over the
1000 Tibetan Plateau, J. Geophys. Res.-Atmos., 106, 18471-18476, doi:10.1029/2000jd900672,
1001 2001.

1002 Zhao, Y., Jiang, Y., Zhang, X., and Lu, X.: Research on the depolarization ratio characteristic of the
1003 aerosol in the atmosphere with the CALIPSO satellite data, Acta Optica Sinaca, 29,
1004 2943-2951, 2009.

1005
1006
1007
1008
1009
1010
1011
1012
1013
1014
1015
1016
1017
1018
1019
1020
1021
1022
1023
1024
1025
1026
1027
1028
1029
1030
1031
1032
1033
1034
1035

1036
1037
1038
1039
1040

1041 Table 1. Refractive indices (R_{eff}) at $0.55 \mu\text{m}$ and effective radius of each size bin for
1042 different aerosol component in SPRINTARS.

Component	$R_{\text{eff}} (\mu\text{m})$										Refractive index
Dust	0.13	0.20	0.33	0.52	0.82	1.27	2.02	3.20	5.06	8.02	$1.530-2.00 \times 10^{-3} i$
BC	0.100	0.108	0.110	0.144	0.169	0.196	0.274	0.312			$1.750-0.440 i$
OC	0.100	0.108	0.110	0.144	0.169	0.196	0.274	0.312			$1.377-3.60 \times 10^{-3} i$
Sea salt	0.178	0.562	1.78	5.62							$1.381-4.26 \times 10^{-9} i$
Sulfate	0.0695	0.085	0.095	0.103	0.122	0.157	0.195	0.231			$1.430-1.00 \times 10^{-8} i$

1043
1044
1045
1046
1047
1048
1049
1050
1051
1052
1053
1054
1055

1056

1057

1058

1059 **Figure Captions**

1060 **Figure 1.** Modeling domains and topography over the vicinity of the TP; the contours
1061 of the terrain height are in km (above mean sea level). The solid black line indicates
1062 the trajectory of the CALIPSO satellite over the TP on 22 August 2007. The black
1063 rectangle indicates the survey region.

1064 **Figure 2.** ~~Column~~-Aerosol optical depth (a), altitude-orbit cross-sections of the total
1065 attenuated backscattering (b) and depolarization ratio (c) on 22 August 2007 along the
1066 trajectory of the CALIPSO satellite over the TP, as presented in Fig. 1. The gray
1067 shading indicates the topography.

1068 **Figure 3.** Daily mean distribution of the (a) AI retrieved from the OMI satellite data
1069 and simulated optical depth of (b) dust aerosols and (c) carbonaceous and sulfate
1070 aerosols from 21 to 23 August 2007.

1071 **Figure 4.** Simulated daily mean distributions of the (a) single scattering albedo and (b)
1072 Angstrom exponent from 21 to 23 August 2007. The black rectangles indicate three
1073 areas of interest.

1074 **Figure 5.** The vertical cross-section of the aerosol extinction coefficient (unit: km^{-1})
1075 from (a) CALIPSO and (b) the simulation by SPRINTARS on 22 August 2007. The
1076 gray shading indicates the topography.

1077 **Figure 6.** Monthly mean aerosol optical depths from the MISR and SPRINTARS
1078 simulations for August 2007.

1079 **Figure 7.** (a) Wind field from ERA-Interim at the 850 hPa level (arrows for the U and
1080 V components of the horizontal wind, units: m s^{-1} ; colors for the vertical wind
1081 velocity, the unit is Pa s^{-1} and the values are negative for updrafts and positive for

1082 downdrafts) from 21 to 23 August 2007. **(b)** Same as **(a)** but for the simulated wind
1083 field at 20 m (units: m s^{-1} , the values of the vertical wind velocity are negative for
1084 downdrafts and positive for updrafts).

1085 **Figure 8.** Cross-section of the **(a)** vertical-longitude and **(b)** vertical-latitude
1086 distributions of the simulated dust mass concentration (units: $\mu\text{g m}^{-3}$) and wind
1087 vectors (shown in arrows; the vertical velocity is multiplied by 10 and 30 for panels **a**
1088 and **b**, respectively) from 21 to 23 August 2007. The gray shading indicates the
1089 topography.

1090 **Figure 9.** Distributions of the simulated dust mass column loading (units: mg m^{-2})
1091 from 21 to 23 August 2007.

1092

1093

1094

1095

1096

1097

1098

1099

1100

1101

1102

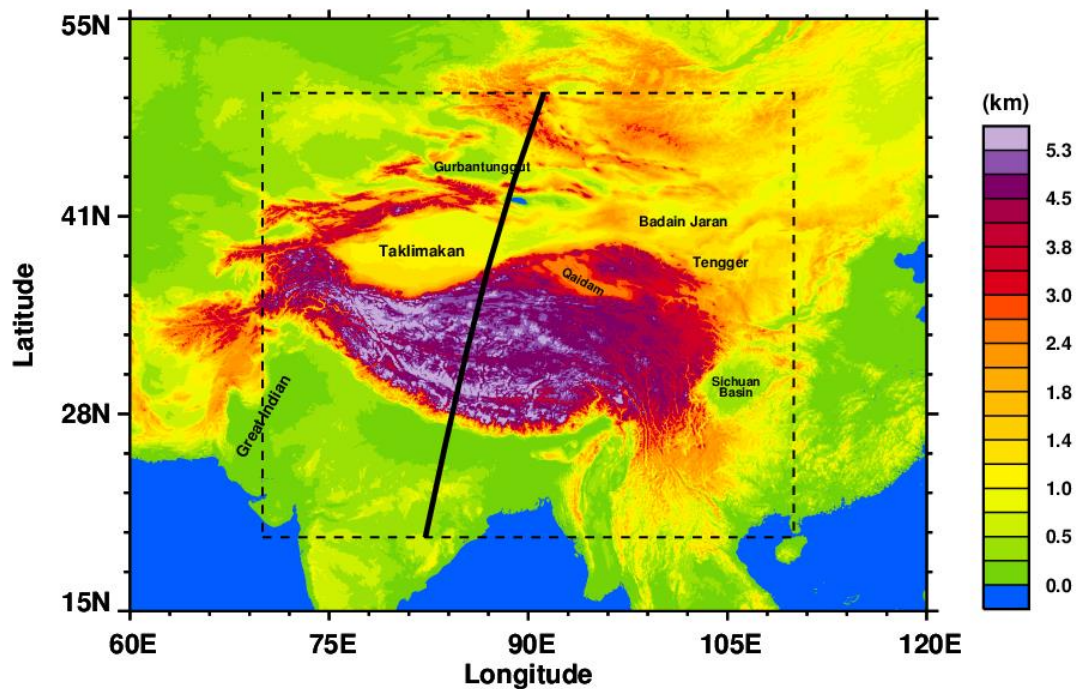
1103

1104

1105

1106

1107
1108
1109
1110
1111



1112

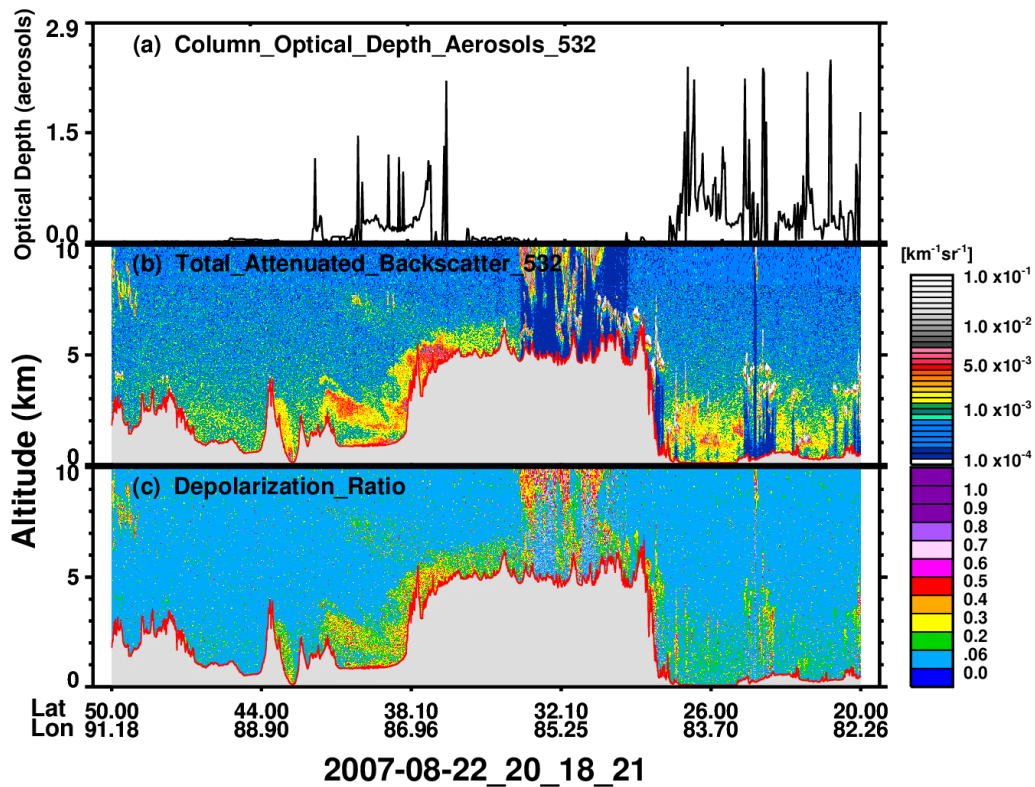
1113 **Figure 1.** Modeling domains and topography over the vicinity of the TP; the contours
1114 of the terrain height are in km (above mean sea level). The solid black line
1115 indicates the trajectory of the CALIPSO satellite over the TP on 22 August 2007.
1116 The black rectangle indicates the survey region.

1117
1118
1119
1120
1121
1122

1123

1124

1125



1126

1127 **Figure 2.** ~~Column~~-Aerosol optical depth (a), altitude-orbit cross-sections of the total
 1128 attenuated backscattering (b) and depolarization ratio (c) on 22 August 2007 along
 1129 the trajectory of the CALIPSO satellite over the TP, as presented in Fig. 1. The
 1130 gray shading indicates the topography.

1131

1132

1133

1134

1135

1136

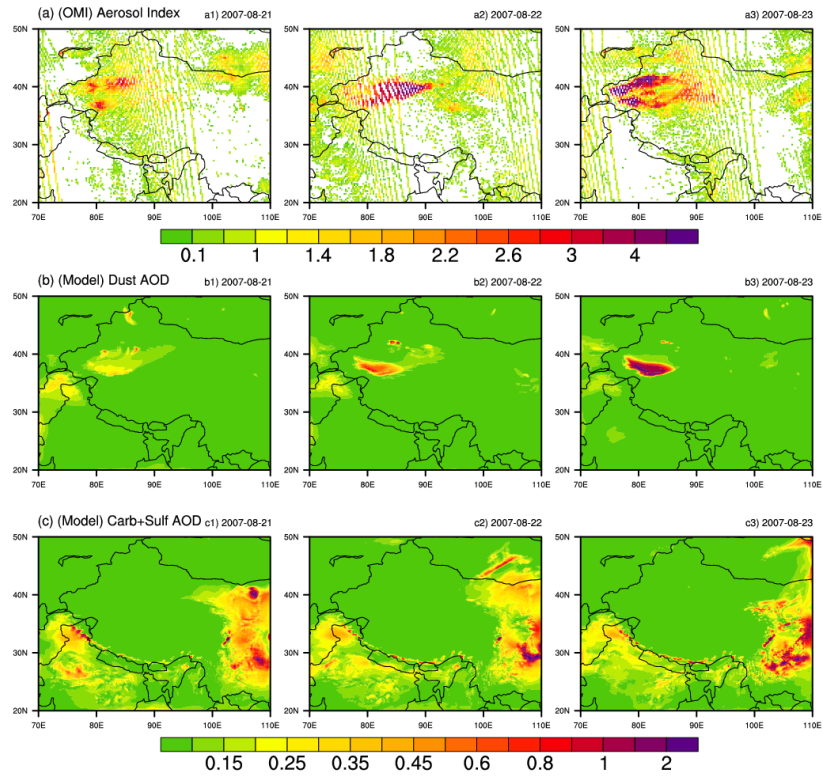
1137

1138

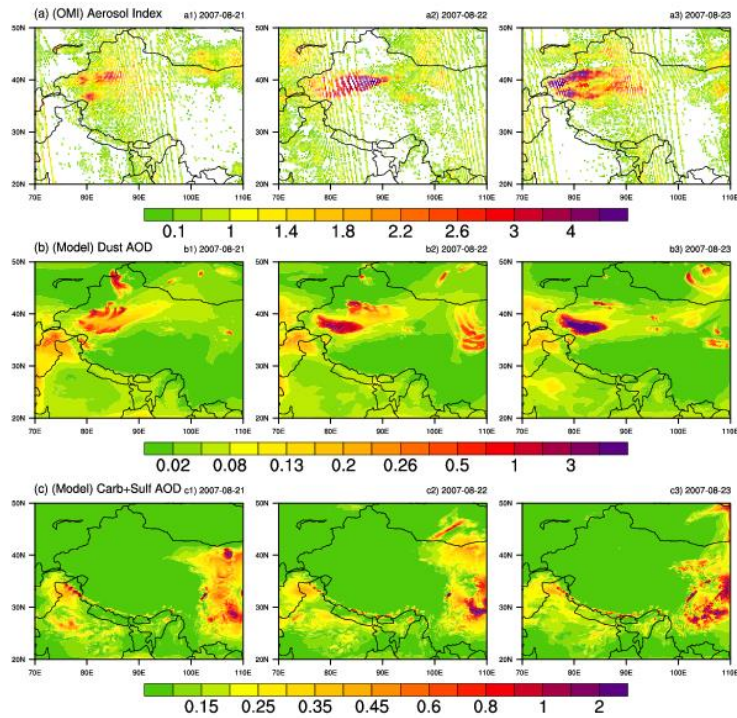
1139

1140

1141



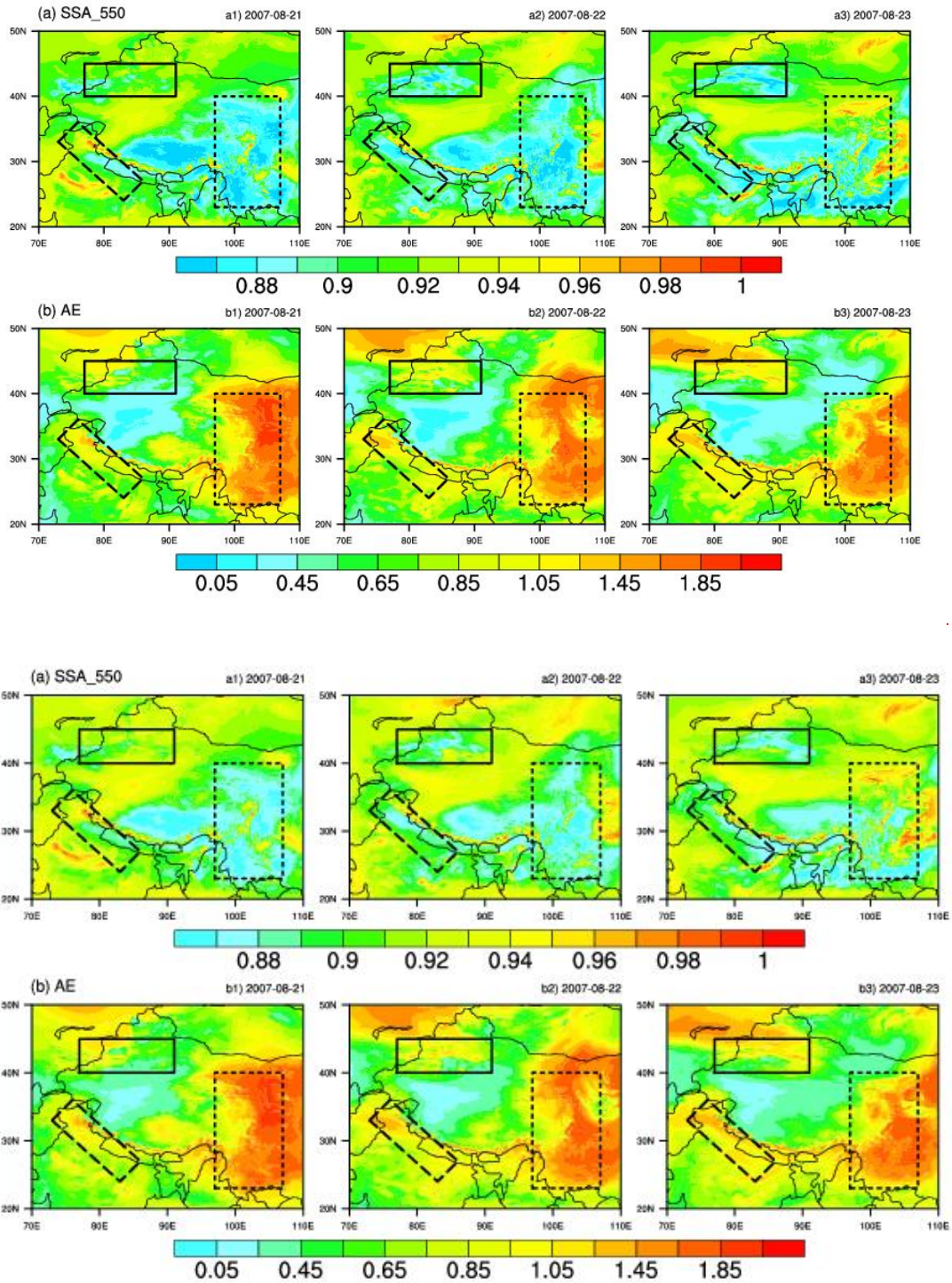
1142



1143

1144 **Figure 3.** Daily mean distribution of the (a) AI retrieved from the OMI satellite data
 1145 and simulated optical depth of (b) dust-aerosols and (c) carbonaceous and sulfate
 1146 aerosols from 21 to 23 August 2007.

1147



1148

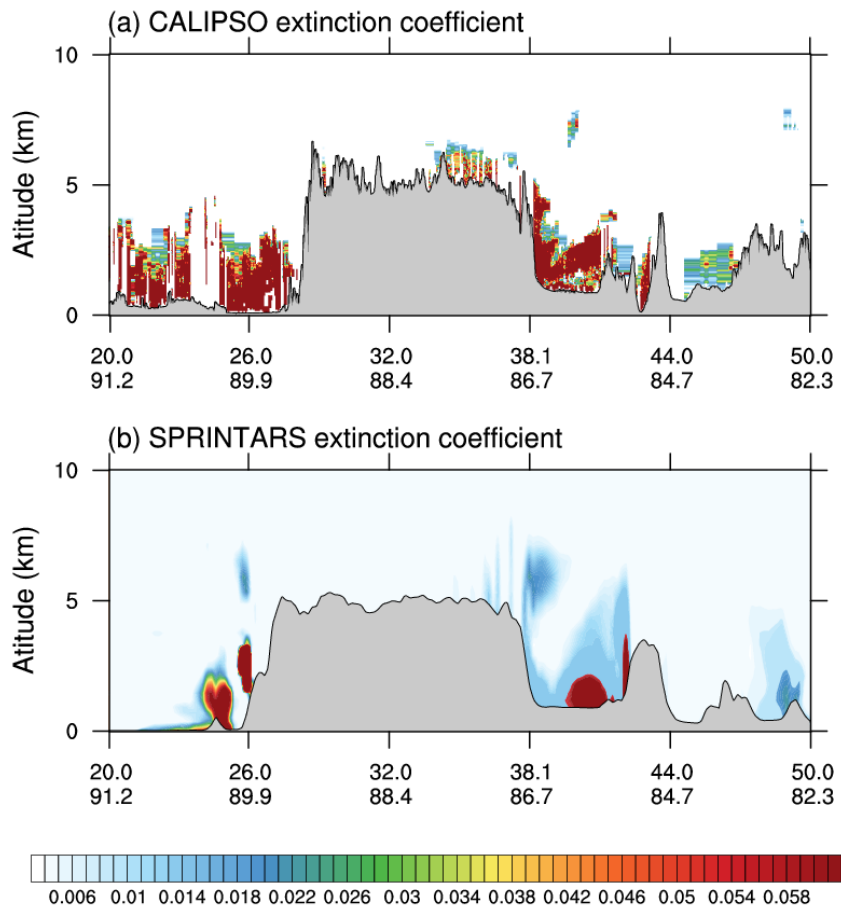
1149

1150 **Figure 4.** Simulated daily mean distributions of the (a) single scattering albedo and (b)
 1151 Angstrom exponent from 21 to 23 August 2007. The black rectangles indicate
 1152 three areas of interest.

1153

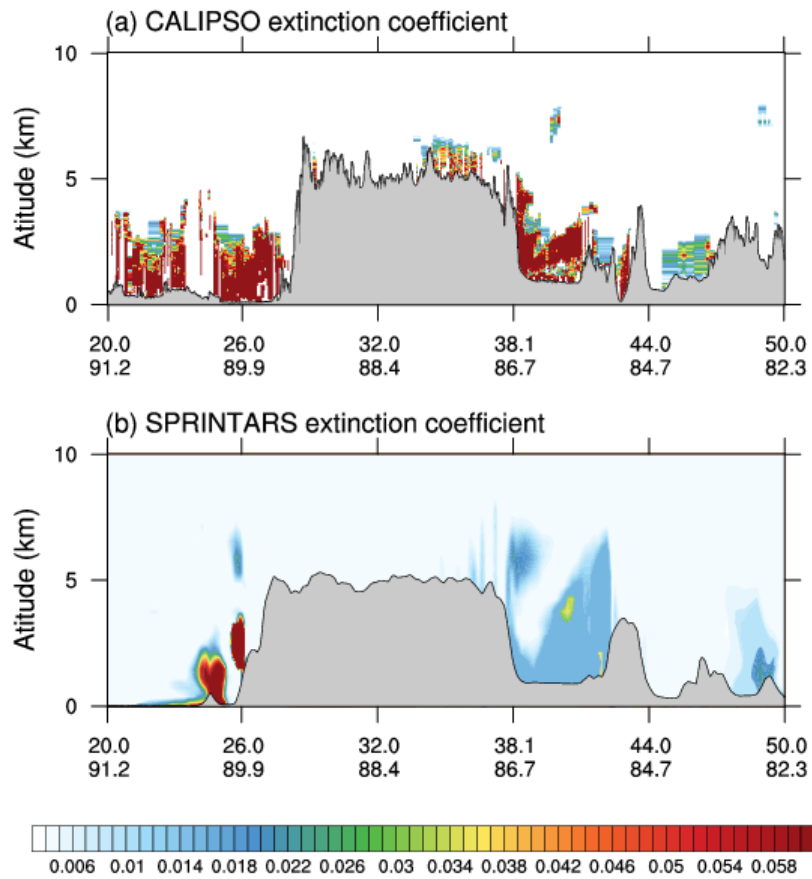
1154

1155



1156

1157



1158

1159 **Figure 5.** The vertical cross-section of the aerosol extinction coefficient (unit: km^{-1})
 1160 from (a) CALIPSO and (b) the simulation by SPRINTARS on 22 August 2007.
 1161 The gray shading indicates the topography.

1162

1163

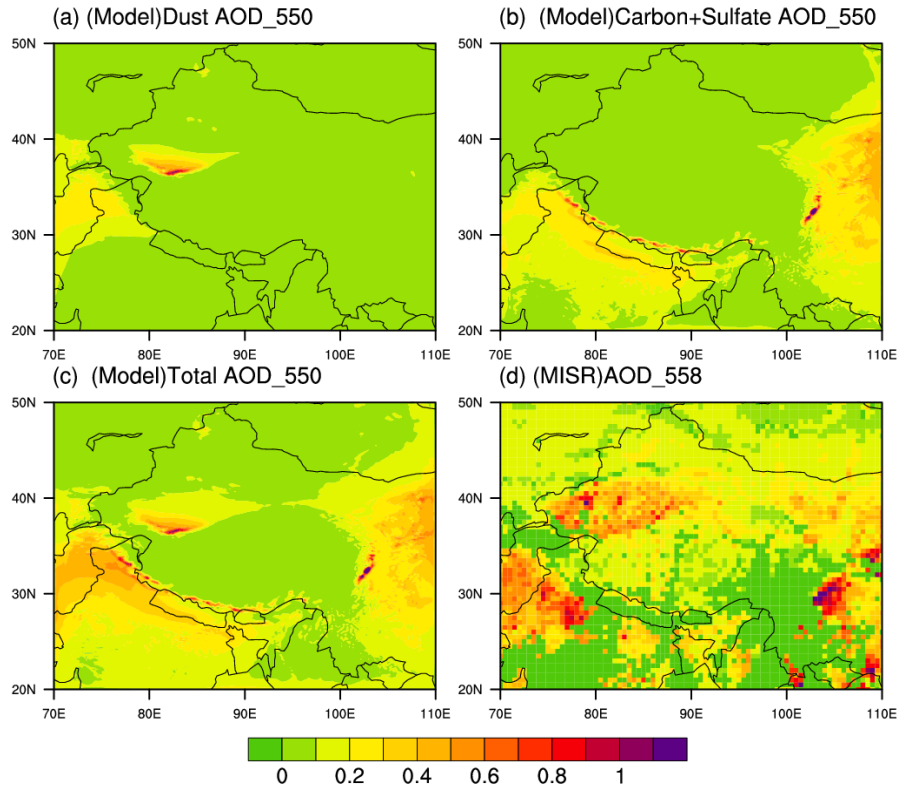
1164

1165

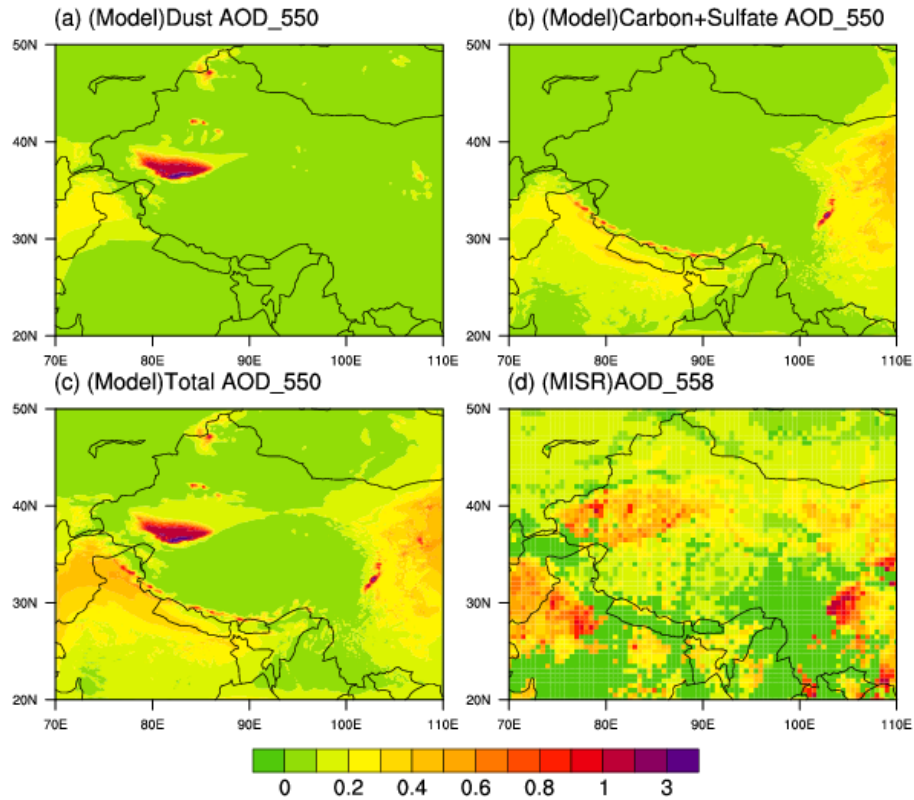
1166

1167

1168



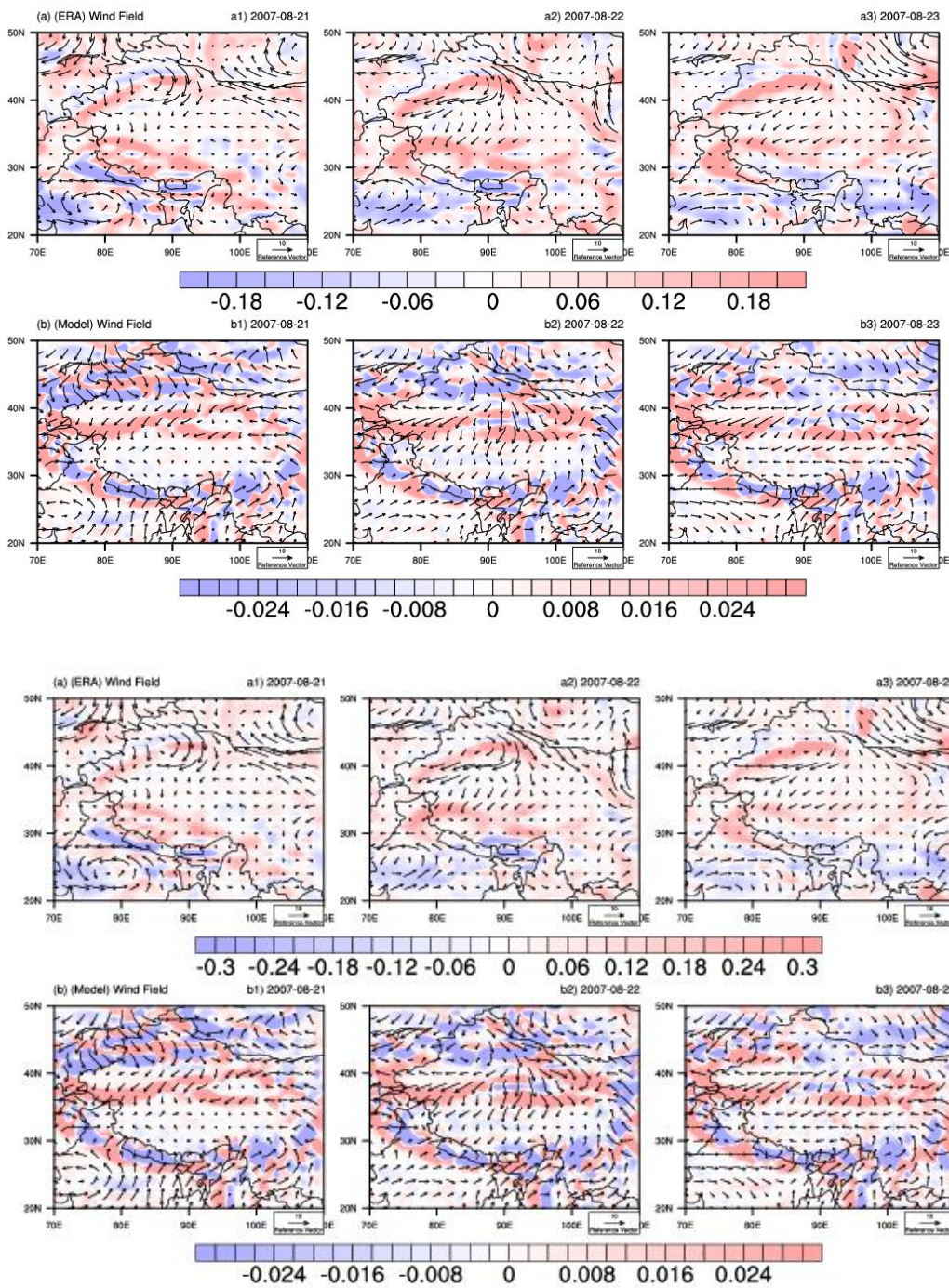
1169



1170

1171 **Figure 6.** Monthly mean aerosol optical depths from the MISR and SPRINTARS
 1172 simulations for August 2007.

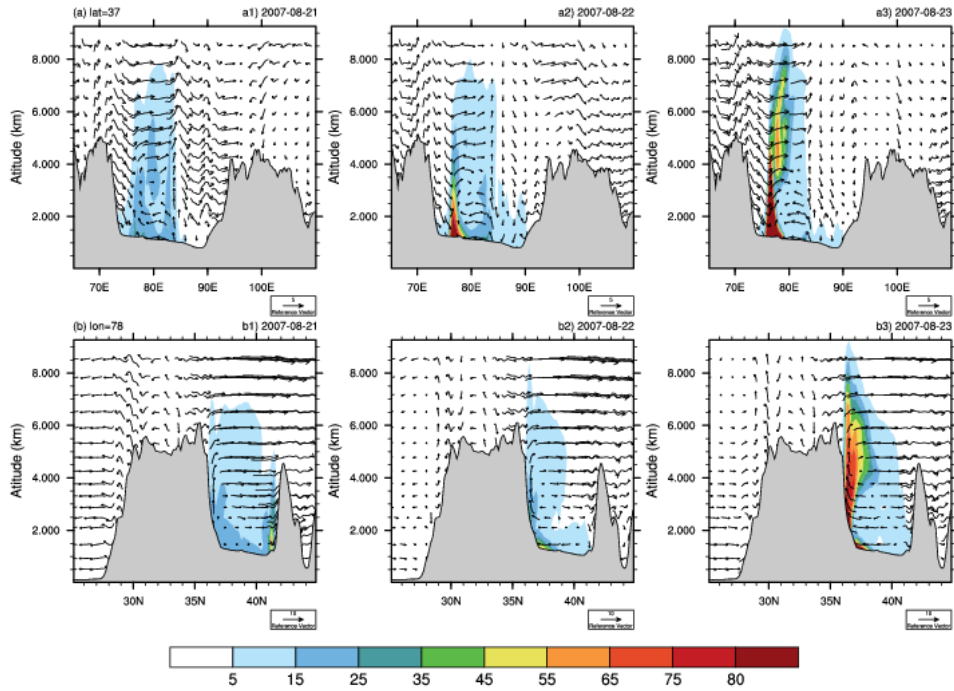
1173



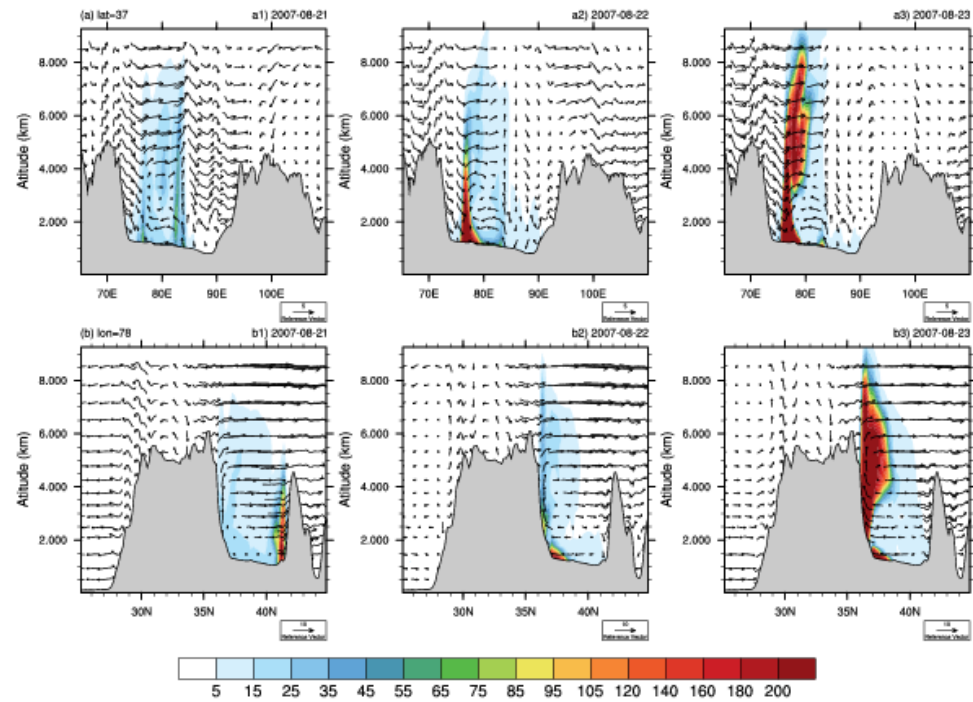
1174

1175

1176 **Figure 7. (a)** Wind field from ERA-Interim at the 850 hPa level (arrows for the U and
 1177 V components of the horizontal wind, units: m s^{-1} ; colors for the vertical wind
 1178 velocity, the unit is Pa s^{-1} and the values are negative for updrafts and positive
 1179 for downdrafts) from 21 to 23 August 2007. **(b)** Same as **(a)** but for the simulated
 1180 wind field at 20 m (units: m s^{-1} , the values of the vertical wind velocity are
 1181 negative for downdrafts and positive for updrafts).



1182

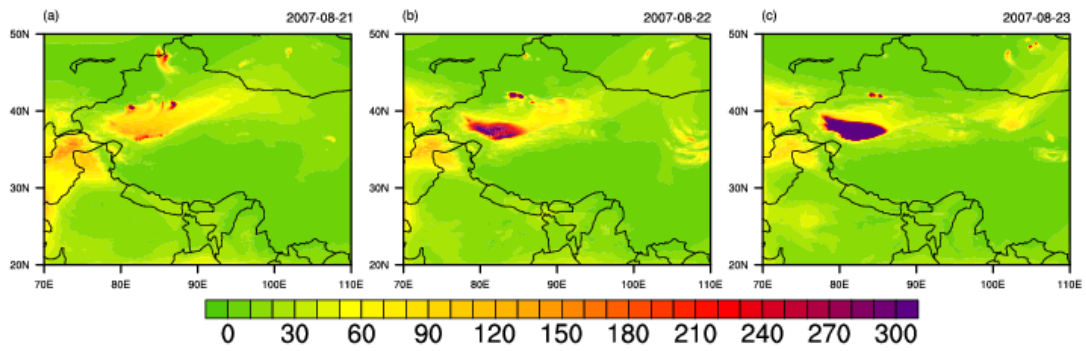


1183

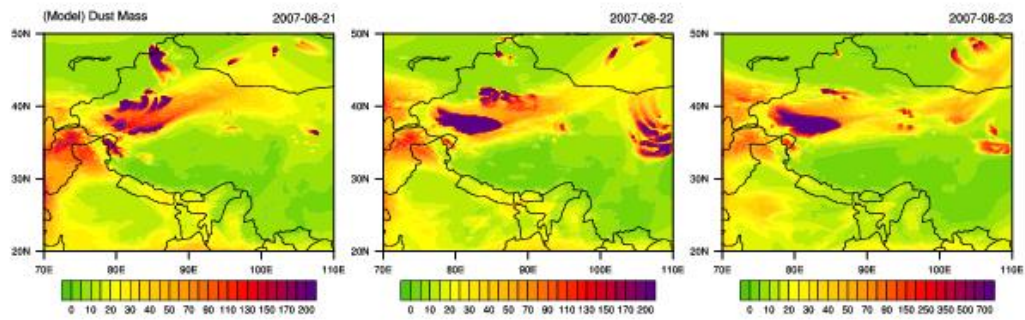
1184 **Figure 8.** Cross-section of the (a) vertical-longitude and (b) vertical-latitude
 1185 distributions of the simulated dust mass concentration (units: $\mu\text{g m}^{-3}$) and wind
 1186 vectors (shown in arrows; the vertical velocity is multiplied by 10 and 30 for
 1187 panels **a** and **b**, respectively) from 21 to 23 August 2007. The gray shading
 1188 indicates the topography.

1189

1190



1191



1192

1193 **Figure 9.** Distributions of the simulated dust mass column loading (units: mg m⁻²)

1194 from 21 to 23 August 2007.

1195